The Origin and Evolution of the Kaapvaal Cratonic Lithospheric Mantle

NINA S. C. SIMON[1]*, RICHARD W. CARLSON[2], D. GRAHAM PEARSON[3] AND GARETH R. DAVIES[1]

[1]FALW, VU AMSTERDAM, DE BOELELAAN 1085, 1081HV AMSTERDAM, NETHERLANDS

[2]DEPARTMENT OF TERRESTRIAL MAGNETISM, CARNEGIE INSTITUTION OF WASHINGTON, 5241 BROAD BRANCH ROAD N.W., WASHINGTON, D.C. 20015, USA

[3]DEPARTMENT OF EARTH SCIENCES, DURHAM UNIVERSITY, SOUTH ROAD, DURHAM DH1 3LE, UK

RECEIVED MARCH 15, 2006; ACCEPTED NOVEMBER 17, 2006; ADVANCE ACCESS PUBLICATION JANUARY 9, 2007

A detailed petrological and geochemical study of low-temperature peridotite xenoliths from Kimberley and northern Lesotho is presented to constrain the processes that led to the magmaphile element depletion of the Kaapvaal cratonic lithospheric mantle and its subsequent re-enrichment in Si and incompatible trace elements. Whole-rocks and minerals have been characterized for Re–Os isotope compositions, and major and trace element concentrations, and garnet and clinopyroxene for Lu–Hf and Sm–Nd isotope compositions. Most samples are characterized by Archaean Os model ages, low Al, Fe and Ca contents, high Mg/Fe, low Re/Os, very low (<0·1 × chondrite) heavy rare earth element (HREE) concentrations and a decoupling between Nd and Hf isotope ratios. These features are most consistent with initial melting at ~3·2 Ga followed by metasomatism by hydrous fluids, which may have also caused additional melting to produce a harzburgitic residue. The low HREE abundances of the peridotites require that extensive melting occurred in the spinel stability field, possibly preceded by some melting in the presence of garnet. Fractional melting models suggest that ~30% melting in the spinel field or ~20% melting in the garnet field followed by ~20% spinel-facies melting are required to explain the most melt-depleted samples. Garnet Nd–Hf isotope characteristics indicate metasomatic trace element enrichment during the Archaean. We therefore suggest a model including shallow ridge melting, followed by metasomatism of the Kaapvaal upper mantle in subduction zones surrounding cratonic nuclei, probably during amalgamation of smaller pre-existing terranes in the Late Archaean (~2·9 Ga). The fluid-metasomatized residua have subsequently undergone localized silicate melt infiltration that led to clinopyroxene ± garnet enrichment. Calculated equilibrium liquids for clinopyroxene and their Hf–Nd isotope compositions suggest that most diopside in the xenoliths crystallized from an infiltrating kimberlite-like melt, either during Group II kimberlite magmatism at ~200–110 Ma (Kimberley), or shortly prior to eruption of the host kimberlite around 90 Ma (northern Lesotho).

KEY WORDS: *Kaapvaal craton; lithospheric mantle; metasomatism; Nd–Hf isotopes; Re–Os isotopes*

INTRODUCTION

Considerable progress has been made in the understanding of craton structure and history in recent years by integrating geophysical and geochemical data. Tomographic studies (e.g. James & Fouch, 2002) and Os isotope analysis of mantle xenoliths (e.g. Walker *et al.*, 1989; Pearson *et al.*, 1995*a*; Carlson *et al.*, 1999; Menzies *et al.*, 1999; Irvine *et al.*, 2001) from the Kaapvaal craton of southern Africa have confirmed and extended models for a thick, cold, lithospheric mantle root (e.g. Boyd & Nixon, 1973; Boyd & McCallister, 1976; Boyd & Gurney, 1986) by delineating the craton boundaries at depth and confirming the Archaean age of much of this ~200 km thick keel. The mechanisms responsible for the formation, consolidation and modification of the cratonic lithosphere remain more controversial (Jordan, 1978; De Wit *et al.*, 1992; Griffin *et al.*, 2003*b*; Schmitz *et al.*, 2004). Perhaps the most important feature of Archaean continental lithospheric mantle (CLM) is that its major element composition

*Corresponding author. Present address: Physics of Geological Processes, University of Oslo, PO Box 1048—Blindern, 0316 Oslo, Norway. Telephone: +47-22856922. Fax: +47-22855101. E-mail: n.s.c.simon@fys.uio.no

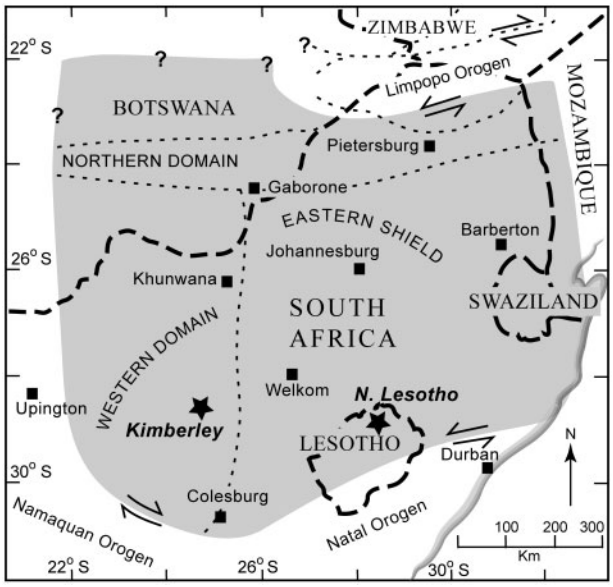

Fig. 1. Simplified geological map modified from Schmitz (2002). The dashed line between Colesburg and Gaberone denotes the Colesburg magnetic lineament, interpreted to mark the suture between the Eastern and Western Kaapvaal blocks. Note the location of Kimberley west of the suture and the position of northern Lesotho close to the southern edge of the craton.

indicates that it is the residue of extensive partial melt extraction. Compared with melt residua produced in experiments, however, many samples of ancient CLM, and in particular the peridotites of the Kaapvaal and Siberian cratons, have unusually high Si/Mg and associated high modal orthopyroxene (opx) contents. The cause of the silica enrichment in Kaapvaal and Siberian low-temperature (low-T: <1150°C) peridotites remains contentious. One model attributes Si enrichment to melting-related processes including addition of cumulate opx at high pressure and temperature in plumes rising from the deep mantle during the initial formation of cratons (Herzberg, 1999; Griffin *et al.*, 2003*a*). The competing explanation is that the CLM peridotites are residua of low-pressure melting and that the Si enrichment is a signature of later enrichment events (e.g. Kesson & Ringwood, 1989; Rudnick *et al.*, 1994; Kelemen *et al.*, 1998).

To better understand the formation and modification processes of continental lithosphere, we present new whole-rock Re–Os isotope and whole-rock and mineral major and trace element and Nd and Hf isotope data for 26 low-T peridotite xenoliths from Kimberley in the centre of the western Kaapvaal craton (Fig. 1). These data are compared with a similar dataset for 19 well-characterized xenoliths from northern Lesotho (Irvine *et al.*, 2001; Simon *et al.*, 2003; Pearson *et al.*, 2004) to address the following questions.

(1) How was the Kaapvaal CLM originally formed? If samples represent residua from melt extraction, when did the melting happen, how much melt was extracted, and under what temperature and pressure conditions did melting occur?

(2) How was the CLM modified over time and what process produced the present-day high modal opx contents of the CLM?

PETROGRAPHIC DESCRIPTION AND CLASSIFICATION

The Kimberley xenoliths were collected from the Old Boshoff Road dump (Bultfontein kimberlite) close to Kimberley, South Africa (Fig. 1). Details of northern Lesotho samples have been given by Irvine *et al.* (2001), Irvine (2002) and Simon *et al.* (2003), who presented the whole-rock major and trace element compositions and modes of these samples. Sample selection focused on fresh samples thought to be representative of the bulk of the Kaapvaal lithospheric mantle; coarse-grained spinel harzburgites and relatively garnet- and clinopyroxene-poor lherzolites (Boyd & McCallister, 1976; Rudnick *et al.*, 1998; James *et al.*, 2004). A few samples that show direct evidence of modal metasomatism, i.e. that contain abundant coarse amphibole and/or phlogopite or veins or clusters of clinopyroxene (cpx) ± hydrous phases, were also collected to cover the more extreme end of the compositional spectrum. Detailed petrographic descriptions are given in Table 1 and photomicrographs can be found in Electronic Appendix 2 online at http://www.petrology.oxfordjournals.org.

Mineral modes for the Kimberley xenoliths were calculated from X-ray fluorescence (XRF) whole-rock major element and electron microprobe mineral data using a least-squares method (Table 2), following the approach of Boyd & Mertzman (1987). Only olivine, opx, cpx, garnet and/or spinel were included in the calculation of modes. Residuals (root mean square; RMS) for calculated modes are usually small (<0·05, Table 2), except for samples rich in minerals other than those used for the regression (e.g. mica and amphibole).

Samples are grouped based on modal mineralogy (Fig. 2) and opx, garnet and cpx morphology and grain-size distribution. This is to emphasize the differences between the samples and facilitate the discussion of the geochemical results by referring to the most extreme 'end-members'.

Type I. This group is composed of refractory harzburgites and lherzolites. It consists of coarse granoblastic to porphyroclastic garnet- and spinel-lherzolites and -harzburgites that generally are texturally equilibrated. The garnet-free samples of this type have the lowest cpx + spinel + garnet contents (<3%) and are characterized by equigranular–interlobate to mosaic olivine crystals, intergrown with varying amounts of opx and minor

Table 1: Petrographic description of thin sections and grouping of the Kimberley and northern Lesotho (Simon et al.*, 2003) samples*

Type	Samples	Description of thin sections	Other classifications
Kimberley			
Type I, gt-free	K2, K6, K8, K9	K2: Inequigranular–interlobate texture dominated by large ol grains (to 1 cm). Opx are much smaller (typically <1 mm, but 0·5 cm porphyroblasts also occur) and often interstitial with strongly lobate grain boundaries. Sp forms rare symplectites with opx and is often altered to magnetite. Opx are clear and no hydrous phases are present	all GP*; 1†
		K6: More altered than K2. Richer in opx and larger opx (to 0·5 cm). Textures are ± equigranular–interlobate (coarse granular) with spinel–opx symplectites. Opx clear, no hydrous phases	
		K8: Coarse granular with more abundant sp symplectites (in part intergrown with cpx) and large (up to 1 cm), mostly clear opx. Some opx show few, fine and sharp exsolution lamellae. No hydrous phases	
Type I gt-bearing	K1, K13, K14, K24, K25, K27, K12, K18, (GP402)	K1: Coarse granular: gt + cpx + opx-rich (<50% ol). <1% phl laths (2 mm). Some strain apparent in form of undulose extinction and subgrain formation in olivine. The texture appears well equilibrated (120° triple junctions common)	GP; 1 or 3
		K13: Large ol crystals (5–10 mm) dominate over subhedral–vermicular opx (poikilitic with ol and gt included), ovoid–vermicular cpx (<1 mm) and mostly round to ovoid gt (0·5–2 mm). Some undulose extinction but no recrystallization., no hydrous phases outside kelyphite	
		K14: similar to K13, but garnets are all round–ovoid and smaller (to 1 mm) and often included in interlobate–vermicular opx. Cpx and ol also occur as inclusions in opx. Cpx also occurs as vermicular grains. Small (<0·1 mm) phl from gt breakdown	GP; 1
		K24: Coarse granular ol–opx (2–5 mm) with smaller (0·5–1·5 mm), remarkably fresh, ovoid garnet and few subhedral–interlobate cpx. Gt often occurs in opx or on opx rims. Cpx is the same size as or larger than garnet and shows thin disrupted exsolution lamellae. Opx can be clear (with undulose extrinction) or cloudy (with exsolution lamellae). No hydrous phases outside kelyphite	GP; 1
		K25: Coarser than K24 and more deformed with some minor foliation. Most ol porphyroclasts are still intact and have very interlobate to amoeboid grain boundaries. Gt are much smaller (1 mm), round-ovoid and often included in opx.No hydrous phases outside kelyphite	GP, 1 or 5
		K27: Coarse granular. Some strain indicated by undulose extinction and initial recrystallization of ol. Ol and opx are slightly larger (1–3 mm) than gt and cpx (0·5–1·5 mm). Gt and cpx are abundant, mostly ovoid, some interlobate, and can form clusters or chains. They are often associated with opx, which can range from subhedral to interlobate in shape, enclosing ol. Opx-rich. No hydrous phases outside kelyphite	GP; 1
		K12: Very altered, beginning recrystallization. Gt have thick black rims and form clusters and chains. Large, clear ol porphyroclasts. Opx have kinked cleavage. Gt-rich areas seem to also have large (mm–cm) opx porphyroclasts. Opx + gt are embedded in a fine-grained (<1mm) recrystallized olivine matrix. Euhedral–subhedral sp (0·1 mm). No hydrous phases	GP; 5
		K18: Deformed. Most ol recrystallized. Round gt, some showing minor resorption on edges, and subhedral to interlobate opx porphyroclasts (0·5–2 and 1–3 mm, respectively). Some huge (cm-size) ol porphyroclasts preserved. Some (<1%) cpx. Gt appears zoned. Deformed phl-veins (<2% whole-rock, but locally abundant) rimmed by small (<0·1 mm) cpx + sp. Phl up to 3 mm	GPP; 4 or 5

(continued)

Table 1: Continued

Type	Samples	Description of thin sections	Other classifications
		GP402: Very fresh coarse granular harzburgite with abundant round–ovoid gt	GP; 1
Type II	K3, K4, K19, K21, (K15, K17)	K3: Slightly strained (undulose extinction in opx), but still granular (1–4 mm). Black alteration veins in ol. Cpx-rich. Garnet is poikilitic. Abundant opaque phases (ilmenite) and inclusions in px and gt. No hydrous phases	GP, GPP, ???; 2, IRPS
		K4: Granular (~1 mm) with small black spinel blebs. Px shapes can vary from subhedral laths to poikilitic-interlobate, with cpx including ol ± opx. Cpx-rich. Few phl (~1 mm, <1%)	GPP?; 2
		K19: Extremely interlobate texture with >3 mm poikilitic gt clusters. It seems that gt formed mainly at the expense of ol, and cpx at the expense of opx. Opx are mostly clear whereas cpx have thin, discontinuous, flasery exsolution lamellae. No hydrous phases	GP?; 2
		K21: Slight strain indicated by undulose extinction and recrystallization of ol. Contains texturally equilibrated phl (to 3 mm, up to 2%). Cpx are vermicular–poikilitic, gt commonly have concave embayments (corroded by cpx + phl forming reaction?). Gt is clouded by either exsolution or inclusion trails	GPP?; 3
		K17: Much finer grained than K19 and K21, especially gt are smaller (<3 mm) and have much more isometric shapes, but can still form clusters and chains. Huge ol (to 1 cm). Opx range from subhedral to vermicular, often enclosing gt and ol. Cpx are small (<1 mm) and often associated with gt–opx clusters. No hydrous phases outside kelyphite	GP?; 1
		K15: Unique sample with interlobate–vermicular gt clusters entirely surrounded by am (5–10%). Coarse (0·5 cm) interlobate opx include ol and have phl on broadened cleavage and cpx on rims. The sample contains black spinel blebs and phl laths in gt mantles within the am. Ol is altered	PKP??; 3
Type III	K7, K10, K11, K16, K20, K22, K23	K7: Coarse (to 1 cm) porphyroclastic. Originally coarse interlobate with poikilitic opx. Opx-rich. Cm-sized blebs of deformed phl with some cpx and am. Network of phl veins. ~30% hydrous phases + cpx. No gt identified in thin section	PP; 3
		K10: Deformed, very altered. Opx porphyroclasts (cm-size) show undulose extinction and subgrain formation. Fine exsolution lamellae are disrupted and kinked. Contains opaque mineral blebs, deformed mica and cpx intergrown with phl + oxides. Opx-rich	PP; 4
		K11: Altered. Blebs of hydrous phases (phl + am) with cpx and oxides, heterogeneously distributed, possibly 2% of whole-rock. Individual, kinked phl laths (0·5–2 mm) Slightly strained, opx shows exsolution	PKP; 3
		K16: Very opx-rich, coarse (0·5–1 cm) equigranular–interlobate. Opx strongly poikilitic and full of phl and sp inclusions along cleavage. Sp–phl–opx–cpx symplectites. Probably was group I sp-harzburgite before hydrous alteration. 10–20% hydrous phases + cpx	PP; 3
		K20: Very coarse grained and equigranular, also initially group I. Now, cm-size opx are cloudy from dense exsolution lamellae/am–phl crystallization along cleavage. Sp–cpx–am symplectites. Very opx-rich	PP–PKP; 3
		K22: Contains cm-sized brown patches of amorphous melt-shaped material, lots of (~10%) cpx and am, all in deformed, partly recrystallized, originally very coarse-grained (0·5 –1 cm) ol matrix. No opx identified	PKP; 3
		K23: Extremely altered, serpentinized. Cm-sized blebs as in K11: Large (3 mm) black sp embedded in cpx, mantled by phl. Cpx:sp:phl = 4:2:1. LIMA minerals. Strained, no gt	PKP; 3 or 4

Lesotho			
Type I gt-free	M5	M5: Fresh, ol-dominated, rel. equant and medium-grained (1 mm), lherzolite with abundant Cr-sp (~3%), commonly interstitial and associated with cpx. Interlobate cpx and opx (some large: 2 mm). Exsolution lamellae in opx oblique to cleavage. No hydrous phases	GP; 1
Type I gt-bearing	LET2, LET38, LET64, GP404, M2, M9, M13, TP5	LET2: Fresh, coarse (3 mm), ol-rich (76%) harzburgite with ~3% purple gt (up to 5 mm), common as inclusion in opx. Grt have two kelyphite rims: inner fine grained and outer coarser phl + sp + px. Opx smaller than ol, irregular interlobate shapes, partly very altered: cracked, cloudy and resorption on grain boundaries and cracks. Some large (>2 mm) subhedral opx preserved. Secondary interstitial sp and ol appear to grow at expense of opx. No hydrous phases outside kelyphite	GP; 1
		LET38: Coarse lherzolite with 0·5–5 mm ol (most large), large (5 mm), subhedral to interlobate to poikilitic opx (36%) with some exsolution lamellae and equally distributed round to ovoid gt (>5%), many entirely kelyphitized. No mica or am	GP; 1
		LET64: Coarse lherzolite, similar to LET38 but fresher, with cpx to 2 mm (<2%), round to ovoid gt (1–2 mm, ~8%) with broad kelyphite rims and ~1% phl laths (up to 5 mm). Contains graphite and kimberlitic glass	GPP; 3?
		GP404 (M): Extraordinarily fresh coarse lherzolite with large (1–5 mm) garnets (~5%) and cpx (2–4 mm, <2%). Bimodal grain-size distribution: <1·5 and >3 mm. Poikilitic opx (mostly large: 5 mm) with round ol inclusions show some exsolution lamella parallel to cleavage. Cpx are clear but have spongy rims and vermicular extensions. <1% phl (up to 0·3 mm) in kelyphite and interstitially	GP; 1 or 3?
		M2: Coarse-grained lherzolite. Mostly >2·5 mm ol and opx (with exsolution lamella subparallel to cleavage) are very clear and fresh. Opx has well-preserved round ol and gt inclusions. Cpx is always cloudy with spongy rims and occurs as single grains (>3 mm), in interstitial veins and attached to gt. Cpx often associated with or enclosing secondary black sp (up to 0·5 mm). Subhedral to slightly irregular gts are fractured and some entirely kelyphitized. <1% up to 1 mm phl laths	GP; 1 or 3?
		M9: Finer-grained (av. 1·5 mm), slightly fractured and serpentinized lherzolite with some large (~5 mm) opx and few large ol. Relatively rich in cracked purple gt (>5%, to 5·5 mm) with up to 0·05 mm thick kelyphite rim that are mantled by sp + phl + cpx aggregates (grain size 0·1–0·3 mm). Abundant cloudy cpx (4%) with spongy rims occurs as single grains, interstitially and in clusters (ol, black sp, phl, cpx) that look like melt pools. <1% phl (1 mm) as individual grains, on gt rims and in the clusters	GPP; 3?
		M13: Ol-dominated (~70%), coarse lherzolite with average grain size of 1 mm and some larger (max. 2·5 mm) ol. Opx is cloudy with many inclusions, irregular shapes, forming an interconnected opx network. 4% of irregularly shaped, dark purple garnet that is partly altered and has (secondary) cpx + phl + sp rims mantling the fine-grained, <0·05 mm kelyphite. Cpx also occurs in veins. Large black secondary sp (0·5 mm) in cpx and opx. Phl–sp–cpx ± gt clusters with disequilibrium textures (<1%)	GPP; 3?
		TP5: Coarse (2–5, av. 3 mm) garnet–spinel lherzolite. Sp occurs in 2px–sp symplectites and as large (0·5 mm) individual grains. Grt-rich (>5%) but inhomogeneously distributed. Garnets partly broken down to px + sp with thick (0·2 mm) black kelyphite rims. Subhedral to anhedral opx, some poikilitic enclosing ol. Ol up to >5 mm. Cpx rare (<2%), small (0·5 mm) and often attached to gt	GPP; 3?

Location abbreviations in sample name: K, Kimberley; M, Matsoku; LET, Letseng-la-Terai; LQ, Liqhobong; TP, Taba Putsoa. Mineral abbreviations: ol, olivine; opx, orthopyroxene; cpx, clinopyroxene; sp, spinel; gt, garnet; phl, phlogopite; am, amphibole; LIMA, lindsleyite-mathiasite solid solution.
*GP (garnet peridotite), GPP (garnet–phlogopite peridotites), PP (phlogopite peridotite) and PKP (phlogopite–K-richterite peridotite) relate to the textural classification of Erlank *et al.* (1987).
†Numbers indicate the peridotite groups defined by Harte (1983). 1, coarse, Mg-rich, cold, granular; 2, coarse, Fe-rich, cold; 3, modally metasomatized, coarse, cold; 4, modally metasomatized, deformed, cold; 5, deformed, Mg-rich, cold. The classification also includes hot deformed peridotite, which was not studied here.

Table 2: Major and minor element and modal compositions of Kimberley whole-rocks

Type:	I (spinel-per.)				I (garnet-per.)								
Sample:	K2	K6	K8	K9	K1	K13	K14	K24	K25	K27	K12	K18	GP402
Major and minor elements (XRF)													
SiO_2	41·37	44·08	43·74	42·32	45·82	43·87	44·38	43·59	44·93	44·35	43·97	42·00	43·28
TiO_2	0·00	0·00	0·00	0·00	0·02	0·01	0·02	0·01	0·01	0·01	0·01	0·06	0·00
Cr_2O_3	0·25	0·34	0·30	0·29	0·38	0·37	0·34	0·34	0·35	0·39	0·49	0·36	0·34
Al_2O_3	0·50	0·80	0·91	0·50	1·68	1·17	1·29	1·59	1·44	1·49	1·47	1·18	2·25
Fe_2O_3(m)	2·48	1·86	2·23	3·28	1·02	2·42	2·40	1·83	1·59	0·91	2·49	2·34	1·40
FeO(m)	3·99	4·15	3·98	3·23	5·05	4·42	4·38	4·96	4·49	5·78	3·34	3·17	4·20
MnO	0·11	0·11	0·11	0·11	0·12	0·12	0·12	0·12	0·11	0·12	0·11	0·10	0·10
MgO	44·69	43·06	43·02	41·82	41·03	41·97	42·20	42·42	40·37	40·60	41·43	43·48	42·09
CaO	0·32	0·28	0·45	0·39	0·96	0·85	0·89	0·97	0·80	1·09	0·59	0·47	0·68
Na_2O	0·04	0·03	0·04	0·17	0·12	0·10	0·08	0·07	0·08	0·07	0·08	0·06	0·06
K_2O	0·01	0·00	0·01	0·04	0·08	0·02	0·07	0·03	0·02	0·01	0·03	0·13	0·04
P_2O_5	0·03	0·02	0·02	0·04	0·03	0·04	0·05	0·04	0·03	0·03	0·05	0·03	0·00
LOI	5·98	5·1	5	7·74	3·63	4·54	3·68	3·92	5·28	4·92	5·61	6·11	5·35
Total	99·52	99·49	99·51	99·64	99·56	99·53	99·56	99·55	99·15	99·38	99·18	99·13	99·45
Sr (XRF)	53	43	47	83	47	58	80	50	51	49	61	43	47
V (XRF)	16	19	14	20	24	25	28	25	23	28	20	16	20
Zr (XRF)	13	9	11	11	19	15	17	14	15	12	20	15	11
Cr (XRF)	1730	2342	2044	1976	2593	2543	2335	2323	2389	2651	3342	2446	2342
Co (XRF)	111	96	105	104	94	105	94	99	85	93	85	91	97
Ni (XRF)	2947	2782	3400	3013	2326	2920	2950	2810	2672	2838	2790	2539	2565
Mg-no.(ol)	92·9	93·0	93·1		92·9	92·2	92·0	92·3	92·9	92·0		93·6	93·6
Modes													
olivine	80	65	65		55	64	64	68	56	61		70	63
opx	19	34	32		35	28	28	22	35	30		19	24
cpx	1·3	0·9	1·7		2·5	2·1	2·1	2·3	1·7	2·8		0·6	2·7 (?)
spinel	0·5	0·6	1										
garnet					7·6	5·7	5·7	7·4	6·8	7·1		10·2	10·4
r.m.s.	0·011	0·044	0·026		0·079	0·051	0·006	0·017	0·079	0·031		0·001	0·028

(continued)

Type:	I–II		II			III							
Sample:	K15	K17	K3	K19	K21	K5	K7	K10	K11	K16	K20	K22	K23
Major and minor elements (XRF)													
SiO_2	43·94	43·16	44·67	43·74	45·05	43·96	45·18	44·07	43·53	44·72	45·33	38·01	40·38
TiO_2	0·07	0·02	0·05	0·05	0·06	0·25	0·06	0·09	0·29	0·02	0·03	0·16	0·13
Cr_2O_3	0·30	0·34	0·50	0·58	0·40	0·37	0·26	0·27	0·34	0·34	0·41	0·23	0·19
Al_2O_3	1·28	1·41	2·05	4·46	2·43	1·44	1·25	0·85	0·48	1·55	1·72	0·79	0·30
Fe_2O_3(m)	2·63	2·94	2·20	2·57	2·52	2·78	1·95	1·60	2·34	2·29	2·32	4·60	3·83
FeO(m)	3·80	3·65	4·88	5·03	4·57	4·97	3·93	4·35	4·12	4·13	3·98	3·51	3·75
MnO	0·12	0·12	0·14	0·18	0·14	0·12	0·10	0·11	0·10	0·12	0·12	0·12	0·12
MgO	40·65	41·53	36·61	36·88	36·45	38·14	40·15	42·51	42·24	40·11	39·58	39·67	41·51
CaO	0·97	0·70	3·68	1·39	2·97	0·75	1·07	0·51	0·71	1·13	1·08	2·36	0·68
Na_2O	0·26	0·08	0·35	0·09	0·29	0·18	0·18	0·14	0·24	0·14	0·24	0·17	0·10
K_2O	0·16	0·02	0·09	0·08	0·21	1·48	0·74	0·48	0·50	1·02	0·23	0·41	0·22
P_2O_5	0·07	0·03	0·06	0·04	0·06	0·04	0·04	0·06	0·04	0·04	0·03	0·06	0·03
LOI	5·31	5·75	4·54	4·85	4·49	5·24	4·85	4·5	4·79	3·97	4·53	9·34	8·15
Total	99·26	99·41	99·32	99·36	99·24	99·35	99·5	99·27	99·38	99·24	99·19	99·2	99·2
Sr (XRF)	136	40	144	62	144	141	83	69	120	104	86	106	49
V (XRF)	22	26	45	29	45	31	27	19	22	30	29	32	19
Zr (XRF)	22	20	24	19	19	49	19	20	106	12	14	14	32
Cr (XRF)	2035	2306	3439	3958	2768	2519	1798	1860	2313	2330	2829	1553	1272
Co (XRF)	99	95	87	89	85	97	82	92	95	95	87	121	90
Ni (XRF)	2711	2826	2334	2258	2327	2406	2492	2724	2876	2787	2474	3024	2893
Mg-no.(ol)	92·5	92·9	87·9	91·2	91·1			92·8	92·1	92·0	92·4		91·6
Modes													
olivine	57	65	56	50	49			63	64	52	48		71
opx	33	26	24	27	29			34	32	41	45		24
cpx	2·14	1·4	18·8	2·1	12·2			1·9	2·8	4·6	4·3		2·8
spinel								0·6	0·8	2·8	3		
garnet	7·4	7·5	1·4	21	9·6								
r.m.s.	0·356	0·143	1·746	0·017	0·001			0·036	0·034	0·142	0·135		0·765

Fe_2O_3(m) and FeO(m) are measured ferric and ferrous iron concentrations (determined by titration). r.m.s., residual mean square of regression.

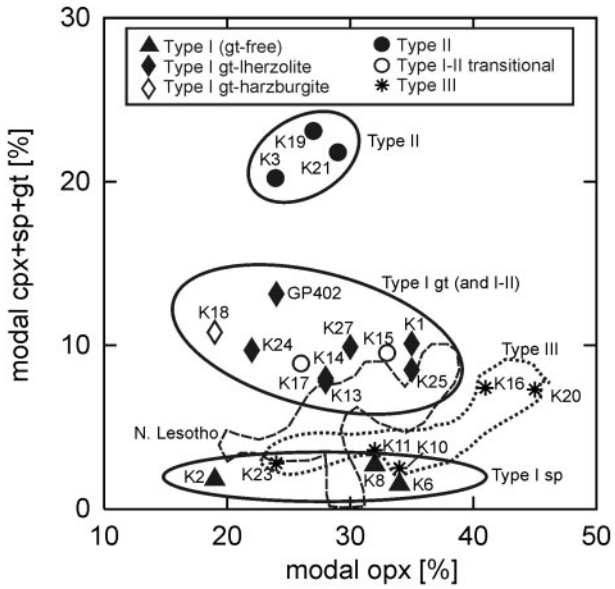

Fig. 2. Calculated modal opx (wt%) vs modal cpx + spinel + garnet (wt%). Opx, orthopyroxene; cpx, clinopyroxene; sp, spinel; gt, garnet. The range of modal composition for the northern Lesotho xenoliths is indicated by the dashed line.

amounts of other phases [see Boyd *et al.* (1999) for a detailed description of similar spinel-facies peridotites]. Opx crystals range in shape from interstitial vermicular (K2, K9) to centimetre-size tabular grains (K20), often showing exsolution lamellae and spinel–opx or spinel–cpx symplectites on opx rims. Generally, the size of opx increases with increasing modal opx. Some opx are poikilitic, enclosing round to ovoid olivine grains, and can have vermicular extensions, giving them a melt-like appearance. Samples may show minor deformation and contain traces of hydrous minerals.

Garnet-bearing Type I samples have variable modal mineralogies (Table 2, Fig. 2) and some contain minor phlogopite and/or amphibole (<1%). Large (millimetre- to centimetre-size) interlobate olivine and opx coexist with ≤4% cpx and ≤10% garnet. Opx vary in shape from large subhedral tabular grains to interlobate, vermicular and poikilitic (including olivine, garnet and cpx) crystals. Garnet grains display isometric–subhedral to ovoid shapes and often appear to be spatially associated with opx (on opx rims, surrounded by or included in opx). Round garnet grains sometimes have concave embayments, probably indicating resorption. Cpx can also be round to ovoid or have very irregular vermicular shapes.

Type II. Defined by garnet- and/or cpx-rich samples K3, K4, K19 and K21, these samples are coarse lherzolites like Type I samples, but are not texturally equilibrated. They contain much more cpx + spinel + garnet (>20%) than the other types. Cpx alone constitutes more than 12% in K21 and K3 (Fig. 2). Garnet (especially in K19) and cpx (in K21 and K4) form clusters and chains of irregularly shaped, vermicular grains, surrounding and overgrowing other minerals. Garnet and cpx grain sizes approach or even exceed those of olivine and opx (<0·5 mm). K3 is a cpx-rich lherzolite, which is very distinct compared with all other samples. Mineral grains in K3 contain abundant inclusions of silicates and opaque phases (mainly spinel and ilmenite). K3 resembles xenoliths of the IRPS (Ilmenite–Rutile–Phlogopite–Sulphide) suite described from the Matsoku kimberlite pipe in northern Lesotho (Harte *et al.*, 1987).

Type III. This type is characterized by higher abundance of hydrous minerals and/or alteration compared with the other types. Some Type III samples appear to be metasomatized former Type I rocks and are roughly equivalent to the phlogopite peridotites (PP) or phlogopite–K-richterite peridotites (PKP) of Erlank *et al.* (1987).

All samples contain tiny (<10 μm) cpx, phlogopite, amphibole and spinel crystals in cracks and along grain boundaries. Garnets usually have thin (maximum 0·1 mm) kelyphite rims. Samples may contain other late-stage secondary and/or alteration products such as calcite, barite, sulphides, etc. These features can be related to the infiltration of host kimberlite during eruption, or to weathering and alteration of the samples at the surface. The effects of these late-stage processes are clearly distinguishable from pre-eruption metasomatism.

ANALYTICAL METHODS

XRF, solution inductively coupled plasma mass spectrometry (ICP-MS) and Re–Os isotope analyses were performed on fractions of 100–500 g (depending on hand-specimen size) powdered bulk-rock. Electron microprobe (EPMA), ion probe (secondary ionization mass spectrometry; SIMS) and laser ablation (LA) ICP-MS analyses were carried out *in situ* on polished thick sections. Typically 1–4 thick sections were prepared per sample, depending on sample homogeneity.

XRF analyses for major elements, Sr, Zr, Cr and V were carried out on 0·4 g of rock powder by S. Mertzman at the Department of Geology, Lancaster, PA, USA. The procedures for the XRF analyses, ferrous iron titrations and loss on ignition (LOI) determinations have been described by Boyd & Mertzman (1987).

Whole-rock trace element concentrations were determined by ICP-MS on ~100 mg of dissolved sample using the HP4500 Plus system at the Vrije Universiteit (VU) Amsterdam. A 10 ppb indium spike was added as an internal standard. The solutions were analysed up to three times and results averaged. A blank was measured at the beginning of each session. Abundance determinations were carried out by peak-height comparison with

a solution of BHVO-2 (US Geological Survey Certificate of Analysis, 1998). Drift corrections were made by recalculating the measured values to literature-defined values (Eggins *et al.*, 1997). MAG-1 (USGS standard sediment) was used as an internal standard. Most elements are reproducible to better than 5% and errors in inter-element ratios are better than 2%. The ICP-MS system was calibrated before the start of each session. Errors on sample analyses based on counting statistics (1σ) are smaller than 10% for light rare earth elements (LREE), high field strength elements (HFSE), Pb, Th, U, Ba, Cs, Y and Sr, and usually <50% for heavy REE (HREE). The 1σ standard deviations on HREE can increase to >100% for very low concentration samples such as Type I spinel harzburgite K6.

Mineral major element compositions were determined by electron microprobe at the Vrije Universiteit Amsterdam using a Jeol JXA-8800 system following Simon *et al.* (2003). Mineral compositions presented in Electronic Appendix Table A (http://www.petrology.oxfordjournals.org) represent averages obtained from 5–20 individual analyses.

Trace element contents in garnet, cpx and opx were measured by LA-ICP-MS at the University of Utrecht (most samples) or by SIMS (K18) at the Department of Terrestrial Magnetism, Washington, DC (DTM). Analytical procedures have been described in detail by Simon *et al.* (2003). Generally no trace element zonation could be detected. The concentrations are therefore average values of several ablation pits (1–5) on different grains (1–5). Where core and rim compositions differ significantly (e.g. in some opx), mineral core and rim compositions are presented separately (Table 3). Opx trace element analyses were complicated by a lack of fresh opx, exsolution lamellae, amphibole or phlogopite films on cleavage planes, and low trace element concentrations. We carefully selected spots for analysis and monitored the changes in concentration of critical elements (Ba, Sr, Nb, Ca) during ablation. Nevertheless, time-resolved analyses occasionally showed spikes in the signal intensities of these elements during analysis. Analyses showing these spikes have been eliminated, to minimize the effect of included phases on the opx analyses. Several trace element abundances in Kimberley opx are very close to, or even below, detection limits. Consequently, the observed variations in middle REE (MREE) and HREE (Eu–Lu), Ba, Y and sometimes Hf in opx are not statistically significant. LREE and large ion lithophile element (LILE) abundances generally exceed analytical errors.

Re–Os isotope analyses were performed on ~1 g aliquots of whole-rock powder using procedures described previously (Carlson *et al.*, 1999). For Nd and Hf isotope analyses, clean and transparent garnets and cpx from selected samples were separated from coarse crush by handpicking. In garnets where trace element zonation was observed we tried to avoid garnet rims by selecting larger fragments surrounded entirely by fresh conchoidal fractures. Minerals were washed in an ultrasonic bath for 15 min in ~5 ml of 4N HCl followed by addition of 0·5 ml of concentrated HF and ultrasonication for another 5 min. The separates were then washed repeatedly in deionized water, re-examined under the binocular microscope and re-picked if necessary. Mineral dissolution and element separation were carried out using techniques described by Carlson *et al.* (2004). Nd and Hf separation and analysis of a subset of samples were performed at the University of Durham by Geoff Nowell (see Dowall *et al.*, 2003; Pearson & Nowell, 2006, for analytical techniques). Sm and Nd isotope analyses on some samples were also carried out by thermal ionization mass spectrometry at the VU Amsterdam. Several mineral separates were analysed in both laboratories (DTM and VU) as a measure of inter-laboratory consistency. All mineral isotope data and the respective techniques and analysis locations are summarized in Table 4.

RESULTS

Pressure–temperature conditions and depth of sampling

Pressures and temperatures were calculated for core and rim compositions of constituent minerals using a range of geothermometers and barometers (Table 5). The different thermometers agree within error for most garnet-bearing Type I samples [for an extensive review on mantle geothermobarometry, see Smith (1999)] and yield temperatures between 900 and 1100°C at 3–4·5 GPa. With the exception of GP402, they fall on a P–T trend consistent with the average Kalahari geotherm of Rudnick & Nyblade (1999; Fig. 3). Type II samples K19 and K21 show considerable scatter in P–T estimates (Table 5) and tend to have lower equilibrium pressures and temperatures [~850°C and ~3·2 GPa for the combination of P and T from Al-in-opx barometry (Brey & Köhler, 1990) and garnet–olivine Fe–Mg thermometry (O'Neill & Wood, 1979)]. This might indicate disequilibrium between phases in these two samples, which is supported by textural evidence and trace element systematics (see below). The Ca-in-opx and Al-in-opx temperature ranges for Type I spinel peridotites (945–1100°C) overlap with the temperature range obtained for garnet peridotites, whereas Mg–Fe exchange thermometers give much lower temperatures (Table 5). This phenomenon was previously observed by Boyd *et al.* (1999) for Kimberley and Simon *et al.* (2003) for Lesotho spinel peridotites. Despite the extensive geochemical evidence for kimberlite modification of the peridotites discussed below, the mineral major

Table 3: In situ trace element analyses of minerals in Kimberley xenoliths

Sample	Mineral	Comment	Spot size (μm)	Rb	Sr	Y	Zr	Nb	Ba	La	Ce	Pr	Nd	Sm	Eu	Gd
K1	opx	av opx	120	0·16	0·89	0·023	0·59	0·161	0·055	0·032	0·107	0·016	0·065	0·030	0·011	0·02
K13	opx	av opx	120	0·110	1·28	0·015	0·210	0·164	0·54	0·044	0·125	0·018	0·10	0·023	0·005	0·02
K14	opx	rim to cpx	40	1·6	1·49	0·030	0·33	0·41	3·1	0·070	0·200	<0·012	0·090	<0·07	<0·015	<0·05
K14	opx	av cores	120	0·27	0·90	0·020	0·145	0·103	0·25	0·008	0·053	0·020	0·15	0·021	0·007	0·02
K17	opx	core	120	<0·04	0·59	0·030	0·66	0·136	0·036	0·004	0·031	0·010	0·060	0·025	0·008	0·03
K17	opx	rim to gt	120	0·26	1·02	0·034	0·64	0·180	0·23	0·034	0·096	0·020	0·13	0·022	0·006	0·02
K19	opx	av all	120	0·25	1·44	0·032	0·31	0·155	0·33	0·075	0·205	0·028	0·10	0·031	0·006	0·02
K24	opx		120	0·140	1·46	0·006	0·170	0·28	0·59	0·108	0·28	0·029	0·15	0·028	0·004	<0·01
K24	opx	av core	120	0·110	0·81	0·010	0·195	0·202	0·125	0·011	0·061	0·015	0·10	0·019	0·008	0·02
K27	opx	possibly contaminated	40	0·180	1·58	0·008	0·23	0·160	0·120	0·006	0·047	0·006	<0·06		0·008	<0·007
GP402	opx	core and rim	SIMS	0·24	0·46	0·015	0·077	0·119	0·012	0·007	0·028		0·061	0·021	0·005	0·009
K1	cpx	av cpx	120	0·20	334	0·79	41	0·43	0·75	3·1	14·9	3·0	16·6	3·5	0·92	1·69
K3	cpx	av cpx	120		199	5·0	71	0·31	0·38	3·7	16·2	3·0	15·2	3·7	1·20	3·0
K11	cpx	repr. rim	120	<0·1	351	7·8	73	0·130	0·40	3·0	17·6	4·4	26	6·8	1·80	4·2
K11	cpx	cpx av	120	0·39	517	11·1	92	0·220		2·9	18·7	5·5	37	9·5	2·4	6·1
K13	cpx	av cpx	120	0·090	342	0·57	12·5	0·51	0·30	3·7	15·1	3·0	16·2	2·5	0·56	1·09
K13	cpx	max cpx	120	0·090	422	0·86	15·5	0·83	0·30	4·7	19·5	3·7	19·7	2·8	0·62	1·40
K13	cpx	min cpx	120	0·090	269	0·37	8·9	0·33	0·30	1·77	9·2	2·2	12·4	2·2	0·49	0·84
K14	cpx	av rims	40		914	0·55	10·7	2·20	8·7	4·6	22·4	6·0	37	4·4	0·68	2·4
K14	cpx	av cores	120	0·43	801	0·31	5·6	0·185	0·73	2·4	16·3	5·1	34	4·0	0·72	1·54
K17	cpx	av cores	120	0·21	360	1·0	49	1·10	2·5?	4·4	18·5	3·7	19·2	4·1	1·03	2·3
K19	cpx	secondary cpx	40 and 120	0·55	394	2·1	40	1·70	8·6?	17·4	47	6·2	26	4·2	1·07	3·6
K19	cpx	primary cpx	120	0·50	378	1·9	39	1·75	9·05?	17·2	46	6·2	24	3·8	0·90	2·2
K21	cpx	av cpx	120	0·21	474	2·8	46	1·66	11?	15·9	51	7·1	26	3·7	0·98	2·9
K24	cpx	av cpx	120 and 40	0·12	508	0·084	6·3	0·42	0·43	4·7	25	4·5	22	2·3	0·33	1·10
K27	cpx	core	120	0·12	367	0·16	3·8	0·41	0·67	3·7	14·6	2·9	14·8	1·51	0·23	0·73
K27	cpx	rim to opx	40	1·4?	281	0·30	6·3	0·74	0·72	2·3	9·8	2·1	10·9	1·55	0·30	0·72
K1	gt	representative rim	120	0·090	0·43	5·0	98	n.a.	0·06	0·022	0·37	0·21	2·6	2·1	0·87	2·5
K1	gt	av core ($n=4$)	120	0·18	0·48	4·2	91	n.a.	0·03	0·029	0·45	0·22	2·6	1·94	0·84	2·1
K3	gt	av gt	120		0·41	30	93	n.a.		0·024	0·156	0·083	1·12	0·99	0·62	2·9
K13	gt	av gt	120	0·20	0·92	2·8	35	n.a.	0·04	0·048	0·60	0·31	3·4	1·68	0·56	1·37
K14	gt	av gt	120 and 40	0·35	1·09	3·6	28	n.a.	0·15	0·032	0·39	0·29	4·6	2·5	0·76	2·1
K14	gt	minimum	mostly 40	0·30	0·78	2·9	22	n.a.	0·08	0·023	0·31	0·21	3·4	2·0	0·57	1·70
K14	gt	maximum	mostly 120	0·40	1·7	4·4	36	n.a.	0·21	0·041	0·45	0·37	5·9	3·2	1·04	2·7
K17	gt	av cores	120	0·16	0·70	7·3	116	n.a.	0·03	0·032	0·35	0·177	2·2	1·94	0·90	2·4
K17	gt	av rim and incl.	40	0·40	1·9	7·6	126	n.a.		0·032	0·33	0·23	2·4	1·95	0·93	2·2
K19	gt	av cores	120	0·24	0·75	12·2	25	n.a.	0·18	0·076	0·32	0·126	1·07	0·95	0·47	1·54
K19	gt	av rims	40		2·7	14·2	23	n.a.	0·16	0·053	0·29	0·130	1·30	0·94	0·54	1·16
K21	gt	rim, very good	120	<0·7	1·5	19·5	16	n.a.	1?	0·030	0·22	0·100	1·00	0·95	0·48	0·87
K21	gt	zoned? Not very clean?	120	1·3	20?	10·0	10	n.a.	5?	2·5	5·6	0·54	2·5	0·80	0·21	0·84
K24	gt	rim to cpx3	40	<0·3	1·1?	0·59	24	n.a.	<0·1	0·021	0·63	0·21	2·4	1·50	0·29	0·64
K24	gt	av gt cores	120	0·14	0·65	0·73	32	n.a.		0·042	0·77	0·32	3·5	1·60	0·44	0·79
K27	gt		40	<0·6	1·9	2·3	26	n.a.	<0·2	0·080	0·52	0·21	2·5	1·45	0·41	0·80
GP402	gt	all	SIMS	0·64	0·83	2·6	9·6	0·64	0·04	0·076	0·79		3·0	0·83	0·194	0·23
K21	phl	av phl	120	290	209	0·13	2·5	8·4	2336	1·34	2·37	0·25	0·67	0·21	1·88	0·39
K11	am	av am ($n=2$)	120	71	329	0·90	44	4·5	12	3·85	8·55	1·15	4·9	0·88	0·29	0·60

(continued)

Table 3: Continued

Sample	Mineral	Comment	Spot size (μm)	Dy	Ho	Er	Tm	Yb	Lu	Hf	Ta	Pb	Th	U	Ti	Cr
K1	opx	av opx	120	0·01		0·003			0·001	0·015	0·020	0·042	0·001	0·003	156	1977
K13	opx	av opx	120	0·02		0·005	0·001		<0·002	0·016	0·027	0·012	0·010	0·003	30	2168
K14	opx	rim to cpx	40	<0·04	<0·01	<0·02	<0·01	<0·07	<0·008	<0·04	0·020	0·10	0·020	<0·007		
K14	opx	av cores	120	0·009				0·008		0·010	0·008			0·002	12	1943
K17	opx	core	120	0·01				0·006	<0·0008	0·044	0·018	0·009	<0·0011	<0·0010	114	2339
K17	opx	rim to gt	120	0·007				0·005	<0·0006	0·009	0·017	0·025	0·004	0·007		
K19	opx	av all	120						0·001	0·012	0·012	0·019	0·012	0·003	228	1313
K24	opx		120	0·006	<0·001	<0·006	<0·005	<0·02	<0·002	0·008	0·038	0·046	0·013	0·005		
K24	opx	av core	120	0·006						0·009	0·033	0·022	0·001	0·002	36	1560
K27	opx	possibly contaminated	40	0·009					<0·001	<0·007	0·023	0·022	<0·0017	<0·0008	24	1737
GP402	opx	core and rim	SIMS	0·007		0·009		0·006		0·018					7	1530
K1	cpx	av cpx	120	0·41	0·04	0·056	0·003	0·02	0·003	2·05	0·044	0·44	0·036	0·010	174	13269
K3	cpx	av cpx	120	1·61		0·42		0·2	0·02	4·2	0·030	0·36	0·045	0·090	2152	6231
K11	cpx	repr. rim	120	2·3		0·60		0·4	0·05	4·5	<0·007	0·50	0·030	<0·003		
K11	cpx	cpx av	120	3·1		0·91		0·5	0·06	5·9	0·014	0·65	0·083	0·018	1433	26320
K13	cpx	av cpx	120	0·27	0·03	0·056	0·004	0·03	0·004	0·56	0·055	0·61	0·150	0·040	138	12640
K13	cpx	max cpx	120	0·35	0·04	0·090	0·007	0·06	0·005	0·66	0·089	0·82	0·37	0·10		
K13	cpx	min cpx	120	0·160	0·02	0·036	0·002	0·02	0·003	0·43	0·032	0·44	0·024	0·008		
K14	cpx	av rims	40	0·43		0·19		0·09		0·40	0·067	2·13	0·161	0·26		
K14	cpx	av cores	120	0·26		0·12	0·02	0·04	0·003	0·30	0·012	0·85	0·020	0·008	18	8912
K17	cpx	av cores	120	0·55		0·092		0·07	0·007	2·6	0·086	0·52	0·087	0·024	348	13030
K19	cpx	secondary cpx	40 and 120	1·1		0·27		0·3	0·02	1·65						
K19	cpx	primary cpx	120	0·75		0·17		0·10	0·01	1·58	0·083	3·48	0·85	0·098	761	11908
K21	cpx	av cpx	120	0·94		0·26		0·18	0·02	1·79	0·068	2·47	0·87	0·092	660	9040
K24	cpx	av cpx	120 and 40	0·12		0·068	0·01	0·04	0·002	0·32	0·036	0·91	0·040	0·017	6	8741
K27	cpx	core	120	0·11		0·033		0·03	<0·001	0·150	0·028	0·70	0·026	0·009	48	8892
K27	cpx	rim to opx	40	0·15		0·042		0·04	0·005	0·170	0·037	0·59	0·045	0·009		
K1	gt	representative rim	120	1·30	0·21	0·44	0·052	0·35	0·071	1·50	n.a.	n.a.	n.a.	n.a.		
K1	gt	av core ($n=4$)	120	1·10	0·148	0·31	0·041	0·33	0·062	1·43	n.a.	n.a.	n.a.	n.a.	270	26005
K3	gt	av gt	120	5·3	1·25	3·8	0·57	3·8	0·57	1·90	n.a.	n.a.	n.a.	n.a.	2344	12921
K13	gt	av gt	120	0·72	0·114	0·22	0·030	0·40	0·059	0·57	n.a.	n.a.	n.a.	n.a.	198	36888
K14	gt	av gt	120 and 40	1·16	0·144	0·26	0·035	0·28	0·044	0·49	n.a.	n.a.	n.a.	n.a.	24	32045
K14	gt	minimum	mostly 40	0·90	0·110	0·15	0·021	0·23	0·018	0·37	n.a.	n.a.	n.a.	n.a.		
K14	gt	maximum	mostly 120	1·40	0·176	0·37	0·041	0·38	0·070	0·65	n.a.	n.a.	n.a.	n.a.		
K17	gt	av cores	120	1·81	0·28	0·59	0·078	0·70	0·11	1·80	n.a.	n.a.	n.a.	n.a.		
K17	gt	av rim and incl.	40	1·93	0·33	0·60	0·080	0·83	0·15	1·87	n.a.	n.a.	n.a.	n.a.	342	32606
K19	gt	av cores	120	2·4	0·46	1·3	0·20	1·4	0·21	0·25	n.a.	n.a.	n.a.	n.a.	366	17743
K19	gt	av rims	40	2·4	0·54	1·5	0·21	1·7	0·19	0·27	n.a.	n.a.	n.a.	n.a.		
K21	gt	rim, very good	120	2·8	0·70	2·1	0·33	3·9	0·49	0·24	n.a.	n.a.	n.a.	n.a.		
K21	gt	zoned? Not very clean?	120	1·50	0·31	1·0	0·26	1·8	0·35	0·110	n.a.	n.a.	n.a.	n.a.	411	15590
K24	gt	rim to cpx3	40	0·170	0·020	0·080	0·022	0·26	0·034	0·46	n.a.	n.a.	n.a.	n.a.		
K24	gt	av gt cores	120	0·183	0·027	0·11	0·023	0·27	0·055	0·58	n.a.	n.a.	n.a.	n.a.	66	27387
K27	gt		40	0·46	0·100	0·19	0·040	0·50	0·10	0·34	n.a.	n.a.	n.a.	n.a.	162	31628
GP402	gt	all	SIMS	0·21		0·40		0·86	0·19	0·25	n.a.	n.a.	n.a.	n.a.	26	20058
K21	phl	av phl	120		0·034		0·010	0·31	0·051	12·3	41	3·4	3·3	0·10	3372	4949
K11	am	av am ($n=2$)	120	0·30		0·073		0·065		2·3	0·15	0·95	0·10	0·031	3423	8625

All by LA-ICP-MS, except GP402 (SIMS). n.a., not analysed.

Table 4: Garnet and clinopyroxene Sm–Nd and Lu–Hf isotopes

Sample	Method	Sm (ppm)	Nd (ppm)	$^{147}Sm/^{144}Nd$	$^{143}Nd/^{144}Nd_m$	2σ	$^{143}Nd/^{144}Nd_i$	εNd_0	εNd_i	t_{DM} (Ga)
Kimberley										
K1cpx	P54	3·5	16·8	0·12	0·512549	0·000005	0·512476	−1·70	−0·87	1·09
K1gt	P54	2·0	2·7	0·45	0·512602	0·000012	0·512334	−0·66	−3·63	−0·38
K3cpx	P54	4·3								
K3gt	P54	1·0	1·5	0·40	0·512298	0·000010	0·512060	−6·59	−8·98	−0·73
K13cpx	P54	2·2								
K13gt	P54	2·0	4·2	0·28	0·512327	0·000005	0·512161	−6·03	−7·01	−2·00
K17gt	Neptune	1·9	2·2	0·54	0·512847	0·000018	0·512529	4·12	0·18	−0·17
K17cpx	Neptune	4·1	19·2	0·13	0·512610	0·000012	0·512535	−0·51	0·28	1·03
K19cpx	P54	3·7	23·8	0·09	0·512144	0·000004	0·512088	−9·60	−8·43	1·34
K21cpx	Neptune	3·7	26·4	0·09	0·511916	0·000007	0·511866	−14·05	−12·77	1·51
K19gt	P54	0·9	1·1	0·51	0·512690	0·000011	0·512391	1·05	−2·52	−0·27
K21gt	Neptune	1·0	1·0	0·57	0·512165	0·000022	0·511827	−9·19	−13·53	-0·44
K24cpx	Neptune	2·3	21·5	0·07	0·512389	0·000008	0·512350	−4·82	−3·32	0·83
K24gt	Neptune	1·6	3·5	0·28	0·512462	0·000009	0·512297	−3·39	−4·35	−1·76
K27cpx	P54	1·8	16·0	0·07	0·512189	0·000005	0·512150	−8·72	−7·23	1·04
K27gt	P54	1·3	4·4	0·18	0·512035	0·000004	0·511930	−11·72	−11·52	4·85
GP402gt	P54	0·9	3·8	0·14	0·512543	0·000006	0·512463	−1·81	−1·12	1·27
GP402gt	Neptune	0·8	3·0	0·17	0·512591	0·000011	0·512491	−0·88	−0·58	2·07
Lesotho										
LET2gt	Neptune	0·6	4·1	0·09	0·511889	0·000014	0·511834	−14·57	−13·39	1·63
LET38cpx	262	2·6	15·7	0·1	0·512618	0·000007	0·512559	−0·35	0·75	0·78
LET38gt	262	1·6	4·5	0·21	0·512369	0·000010	0·512245	−5·21	−5·38	30·3
LET64cpx	262	3·5	13·9	0·15	0·512589	0·000086	0·512499	−0·92	−0·42	1·5
LET64gt	262	2·1	5·5	0·23	0·512309	0·000026	0·512172	−6·38	−6·79	−8·15
GP404cpx	Neptune	3·5	15·2	0·14	0·512720	0·000011	0·512639	1·64	2·31	0·95
GP404gt	Neptune	1·4	2·4	0·35	0·512487	0·000026	0·512283	−2·91	−4·63	−0·83
GP404gt	262	1	2	0·29	0·512516	0·000031	0·512348	−2·34	−3·36	−1·49
M2cpx	P54	5·7	37·7	0·09	0·512415	0·000005	0·512361	−4·31	−3·1	0·97
M2gt	P54	2·5	5·2	0·29	0·512391	0·000006	0·512221	−4·78	−5·84	−1·69
M5cpx	P54	3·1	8·5	0·22	0·512640	0·000005	0·512512	0·08	-0·15	−67·49
M9cpx	P54	3·7	15·2	0·15	0·512728	0·000007	0·512641	1·78	2·35	1·06
M9gt	P54	1·8	2·1	0·51	0·512851	0·000008	0·512551	4·19	0·6	−0·18
M9gt	Neptune	1·7	2·6	0·39	0·512870	0·000025	0·512642	4·56	2·37	−0·29
M13cpx	262	4·2	20·4	0·12	0·512584	0·000021	0·512511	−1·01	−0·18	1·03
M13gt	262	1·8	5·3	0·2	0·510783	0·000023	0·510664	−36·15	−36·22	25·46
M13gt	Neptune	1·3	4·4	0·17	0·511871	0·000011	0·511769	−14·92	−14·65	4·71
TP5cpx	262	10	53·1	0·11	0·512658	0·000011	0·512591	0·43	1·38	0·82
TP5gt	262	1·2	7·7	0·09	0·512582	0·000009	0·512526	−1·05	0·12	0·78

(continued)

element data appear to record coherent *P–T* information for Type I garnet peridotites, probably because of relatively rapid diffusion of the major elements on which the thermobarometers are based, relative to the slow diffusivities of trivalent trace elements (e.g. Ganguly *et al.*, 1998; Van Orman *et al.*, 2001, 2002).

Major and trace element compositions of the constituent minerals

A detailed description of the Kimberley mineral compositions is provided in Electronic Appendix 1 (available online at http://www.petrology.oxfordjournals.org). Representative major element data for Kimberley

Table 4: Continued

Sample	Method	Lu (ppm)	Hf (ppm)	$^{176}Lu/^{177}Hf$	$^{176}Hf/^{177}Hf_m$	2σ	$^{176}Hf/^{177}Hf_i$	εHf_0	εHf_i	t_{DM} (Ga)	$\Delta\varepsilon Hf$
Kimberley											
K1cpx	P54	0·0038	2·303	0·00023	0·282680	0·000013	0·282680	−3·3	−1·2	0·82	−3·40
K1gt	P54	0·0686	1·744	0·00558	0·282648	0·000016	0·282638	−4·4	−2·7	1·00	−1·27
K3cpx	P54	0·0101	1·357	0·00106	0·283333	0·000015	0·283331	19·8	21·8	−0·05	18·52
K3gt	P54	0·4086	0·1266	0·45878	0·290890	0·000078	0·290092	287	261·0	0·93	269
K13cpx	P54	0·0018	0·5338	0·00048	0·282903	0·000035	0·282902	4·6	6·6	0·53	3·35
K13gt	P54	0·0891	0·6726	0·01880	0·282893	0·000040	0·282860	4·3	5·2	1·04	10·98
K19cpx	P54	0·0094	1·609	0·00083	0·282801	0·000021	0·282800	1·0	3·0	0·67	10·68
K19gt	P54	0·2868	0·2157	0·18883	0·285833	0·000034	0·285505	108	98·7	0·87	98·68
K27cpx	P54	0·0013	0·2205	0·00084	0·283150	0·000032	0·283149	13·4	15·4	0·20	21·46
K27gt	P54	0·0914	0·276	0·04701	0·283831	0·000013	0·283749	37·5	36·6	3·30	48·29
GP402gt	P54	0·2	0·1368	0·20789	0·292841	0·000095	0·292480	356	345·4	2·85	344
Lesotho											
LET38cpx	P54	0·0018	0·825	0·00031	0·282866	0·000015	0·282865	3·3	5·3	0·58	1·83
LET38gt	P54	0·0408	0·4327	0·01339	0·283382	0·000018	0·283359	21·6	22·8	−0·17	27·25
LET64cpx	P54	0·0228	3·719	0·00087	0·282663	0·000023	0·282661	−3·9	−1·9	0·86	−3·86
LET64gt	P54	0·0406	0·2384	0·02418	0·283392	0·000053	0·28335	21·9	22·5	−0·32	28·77
GP404cpx-b	P54	0·0079	1·962	0·00057	0·28282	0·000019	0·282819	1·7	3·7	0·64	0·42
GP404gt	P54	0·0848	0·503	0·02393	0·28329	0·000045	0·283248	18·3	18·9	0·03	20·73
M2cpx	P54	0·004	2·112	0·00027	0·282839	0·000015	0·282839	2·4	4·4	0·61	5·13
M2gt	P54	0·0779	0·5142	0·02152	0·283113	0·000023	0·283075	12·0	12·8	0·55	17·05
M5cpx	P54		2·178	0·00652	0·282404	0·000006	0·282393	−13·0	−11·4	1·41	−14·46
M9cpx	P54	0·0075	3·534	0·00030	0·282698	0·000016	0·282698	−2·6	−0·6	0·80	−3·88
M9gt	P54	0·105	1·605	0·00929	0·282293	0·000015	0·282277	−16·9	−15·5	1·73	−19·54

Total procedural blanks measured for these methods were Sm = 18 pg, Nd = 40 pg, Lu = 43 pg, Hf = 86 pg. For the Finnigan 262 (VU), an exponential fractionation correction was applied using $^{146}Nd/^{144}Nd = 0{\cdot}7219$ and the data were normalized to a La Jolla Nd standard value of $^{143}Nd/^{144}Nd = 0{\cdot}511860$. The in-house IGO standard was analysed only during this session and was within error of the long-term reproducibility of this standard ($^{143}Nd/^{144}Nd = 0{\cdot}511335 \pm 15$, $n = 25$, Heumann, 1999; $^{143}Nd/^{144}Nd = 0{\cdot}511338 \pm 16$, $n = 50$, which is equivalent to a La Jolla value of $0{\cdot}511850 \pm 22$, $n = 43$). For the VG Plasma 54 (DTM), all Nd data are fractionation corrected to $^{146}Nd/^{144}Nd = 0{\cdot}7219$ and normalized to a value of $^{143}Nd/^{144}Nd = 0{\cdot}511860$ for the La Jolla standard. An average of $^{143}Nd/^{144}Nd = 0{\cdot}511821 \pm 17$ ($n = 16$) was obtained for the La Jolla standard. Sm is fractionation corrected to $^{147}Sm/^{152}Sm = 0{\cdot}56081$. Hf data are fractionation corrected to $^{179}Hf/^{177}Hf = 0{\cdot}7325$ and reported relative to a value of $^{176}Hf/^{177}Hf = 0{\cdot}282160$ for Hf standard JMC475. The average measured value for this standard was $0{\cdot}282157 \pm 6$ ($n = 13$) during July 2002, well in agreement with the long-term average ($0{\cdot}282155 \pm 6$, $n = 45$). Decay constants for ^{147}Sm and ^{176}Lu are $6{\cdot}54 \times 10^{-11}$ year^{-1} and $1{\cdot}865 \times 10^{-11}$ year^{-1}, respectively. εNd and εHf were calculated using the following Bulk Earth values: $^{147}Sm/^{144}Nd = 0{\cdot}1966$, $^{143}Nd/^{144}Nd = 0{\cdot}512636$, $^{176}Lu/^{177}Hf = 0{\cdot}0332$, $^{176}Hf/^{177}Hf = 0{\cdot}282772$. $^{147}Sm/^{144}Nd = 0{\cdot}2152$, $^{143}Nd/^{144}Nd = 0{\cdot}5132$, $^{176}Lu/^{177}Hf = 0{\cdot}03893$ and $^{176}Hf/^{177}Hf = 0{\cdot}2833$ were used as depleted mantle parameters for the calculation of Nd and Hf model ages.

samples are presented in Electronic Appendix Table A and the most salient aspects of the data are discussed below. Mineral compositions for northern Lesotho xenoliths were discussed by Simon *et al.* (2003).

Olivine

Olivines in the Kimberley samples have generally homogeneous compositions with mean and median Mg-number [=molar (Mg/(Mg + Fe)) × 100] of 92·4, within error of average cratonic mantle (median 92·1, Pearson *et al.*, 2003).

Orthopyroxene

The opx are enstatites, with mean and median Mg-number (93·2 and 93·3, respectively) usually slightly higher than in the corresponding olivines (Electronic Appendix Table A). The majority of samples show minor compositional variations, restricted to the outermost rims (50 μm). Type I opx are more magnesian (Mg-number 93–94) and Type II are the least Mg-rich (90–92).

Opx have two distinct trace element patterns that seem to be unrelated to the petrographic types (Fig. 4a): (1) sinusoidal REE patterns characterized by depletion

Table 5: Calculated pressures and temperatures for mineral cores and rims

	Garnet-free peridotites																	
Sample:	K2	K2	K6	K6	K8	K8	K4	K4	K10	K10	K11	K11	K16	K16	K20	K20	K23	K23
Position:	symp.	rim	core	rim	core	rim	core	rim	core	rim	core	rim	core	rim	core	rim	core	rim
Type:	I	I	I	I	I	I	II	II	III	III	III	III	III	III	III	III	III	III
T_{PRESET}:	800	800	800	800	1000	1000	1000	1000	800	800	800	800	800	800	700	700	1000	1000
p_{PRESET}:	2·0	2·0	2·0	2·0	2·0	2·0	2·0	2·0	2·0	2·0	2·0	2·0	2·0	2·0	2·0	2·0	4·0	4·0
Thermobarometers, calculated with preset temperature or pressure T *(°C)*, P *(GPa)*																		
T (BKN)	1036	1472	1476	1077	833	1470	885	921	956	1023	944	963	610	638	845	1076	952	958
T (KB)	781	817	1007	610	623	946	807	835	795	938	0	0	674	574	711	978	0	0
T (Wells)	990	855	855	982	882	858	851	901	893	951	885	897	710	722	850	966	876	880
T opx-cpx (BM)	998	1344	1341	1005	830	1343	830	863	905	970	0	0	622	639	803	997	0	0
T Ca-in-opx (BKN)	945	989	939	955	1018	980	786	800	824	854	818	813	737	707	1005	870	905	921
T Na-in-px (BKN)	580	404	390	465	848	414	809	971	911	993	901	920	647	632	1269	907	906	909
T ol-sp (OW)	780	476	673	470	686	698	887	929	968	1005	1010	506	975	975	827	597	1143	582
T Al in opx (WS)	1034	972	1031	970	1082	1044	750	761	780	782			671	666	831	800		
T ol-sp (Bal)	765	518	652	512	665	676	858	897	929	959			933	934	769	602		
	Garnet-bearing peridotites																	
Sample:	K1	K1	K13	K13	K14	K14	K24	K24	K25	K25	K27	K27	K18	K18	GP402	GP402		
Position:	core	rim	core	rim	core	rim	core	rim	core	rim	core	rim	core	rim	core	rim		
Type:	I	I	I	I	I	I	I	I	I	I	I	I	I	I	I	I		
T_{PRESET}:	1000	1000	1000	1000	1000	1000	1000	1000	1000	1000	1000	1000	1000	1000	1000	1000		
p_{PRESET}:	4·0	4·0	4·0	4·0	4·0	4·0	4·0	4·0	4·0	4·0	4·0	4·0	4·0	4·0	4·0	4·0		
Thermobarometers, calculated with preset temperature or pressure T *(°C)*, P *(GPa)*																		
T (BKN)	1042	1581	1060	1003	1004	847	1010	957	1062	1146	1041	1125	1136	1134				
T (KB)	981	1232	1048	1101	1002	1013	1007	1017	1073	1131	1057	1139	1023	1064	1224	1260		
T (Krogh)	1010	11300	1033	1114	935	1051	977	1074	1061	1155	1003	1090	1118	742				
T (O'Neill)	962	968	982	1009	1024	1022	987	992	994	1013	1030	1008	1055	434	1110	1110		
T (Harley)	928	921	949	959	953	972	973	988	985	1014	998	1004	1007	508	1059	1060		
T (EG)	1073	4719	1080	1149	991	1091	1037	1118	1110	1194	1056	1128	1162	778				
T (Pow)	1057	5665	1064	1137	972	1076	1019	1105	1097	1185	1039	1115	1151	755				
T (Wells)	941	850	966	932	952	843	950	910	956	1013	974	1020	983	1003				
T opx-cpx (BM)	980	1366	997	926	962	794	957	888	1000	1076	988	1062	1077	1078				
T Ca-in-opx (BKN)	972	975	1001	1013	975	998	981	1000	970	994	1006	1021	1008	1001	998	1005		
T Na-in-px (BKN)	1040	791	1088	1179	1017	1098	1019	1036	1025	1084	1059	1060	1065	1169	794	781		
P (BKN)	3·98	3·87	3·88	3·83	4·29	4·14	4·11	4·05	3·87	3·55	4·04	3·76	4·01	3·52	2·95	2·90		
P (KB)	4·26	0·14	3·36	2·70	3·98	3·82	3·90	3·77	3·04	2·18	3·24	2·01	3·69	3·15	0·29	−0·29		
P (NG)	4·16	4·08	4·18	4·12	4·42	4·31	4·27	4·21	4·08	3·77	4·25	4·00	4·27	4·56	3·16	3·10		
P (MC)	4·46	4·40	4·52	4·39	4·63	4·54	4·57	4·48	4·48	4·08	4·57	4·30	4·44	4·35	4·43	4·40		
Thermobarometer combinations (solved iteratively) T *(°C)*, P *(GPa)*																		
T (BKN/BKN)	1046	1802	1065	1000	1010	834	1013	953	1066	1153	1047	1135	1151	1135				
P (BKN/BKN)	4·25	8·49	4·27	3·83	4·35	3·13	4·19	3·76	4·25	4·37	4·33	4·55	4·82	4·06				
T (BKN/KB)	1062	2864	1064	975	1005	804	1011	939	1059	1145	1036	1113	1174	1156				
P (KB/BKN)	5·13	30·07	4·21	2·38	4·05	1·13	4·05	2·94	3·81	3·98	3·72	3·40	6·05	5·21				
T (Krogh/BKN)	1012	−7516	1038	1144	929	1078	976	1104	1074	1179	1007	1107	1158	693				
P (BKN/Krogh)	4·05	−45·16	4·11	4·66	3·85	4·62	3·96	4·68	4·29	4·51	4·08	4·39	4·86	2·28				
T (O'Neill/BKN)	946	948	967	1002	1052	1041	989	992	984	989	1045	996	1074	319	1076	1074		
P (BKN/O'Neill)	3·66	3·57	3·69	3·84	4·61	4·39	4·04	4·00	3·78	3·49	4·32	3·74	4·41	0·77	3·29	3·23		
T (Harley/BKN)	891	873	913	923	953	969	967	985	965	979	1001	984	1012	406	989	986		
P (BKN/Harley)	3·34	3·14	3·37	3·38	3·99	3·96	3·91	3·96	3·67	3·43	4·05	3·67	4·08	1·12	2·90	2·83		
T (OpxBK/BKN)	961	960	995	1007	982	1006	981	1003	952	965	1012	1014	1011	975	938	943		
P (BKN/OpxBK)	3·75	3·64	3·85	3·87	4·18	4·18	3·99	4·07	3·60	3·36	4·11	3·84	4·07	3·42	2·67	2·64		

(continued)

Table 5: Continued

Sample:	K15	K15	K17	K17	K19	K19	K21	K21	K3	K3
Position:	core	rim	core	rim	core	rim	core	rim	core	rim
Type:	I-II	I-II	I-II	I-II	II	II	II	II	II	II
T_{PRESET}:	1000	1000	1000	1000	1000	1000	1000	1000	1000	1000
p_{PRESET}:	4·0	4·0	4·0	4·0	4·0	4·0	4·0	4·0	4·0	4·0
Thermobarometers, calculated with preset temperature or pressure T *(°C)*, P *(GPa)*										
T (BKN)			1055	1009	929	963	794	914	1063	1185
T (KB)	1050	1162	946	1008	930	1000	806		1053	1215
T (Krogh)			1035	1151	1005	1037	1280	1491	1050	1132
T (O'Neill)	877	887	1043	1084	889	938	887		1033	1078
T (Harley)	919	934	1020	1051	920	954	928	940	969	981
T (EG)			1093	1192	1072	1097	1302	1467	1114	1184
T (Pow)			1078	1183	1056	1082	1300	1478	1100	1174
T (Wells)			959	926	866	890	741	811	945	1050
T opx–cpx (BM)			1000	938	849	879	916		963	1092
T Ca-in-opx (BKN)	853	854	951	958	877	921	878	890	1019	1018
T Na-in-px (BKN)	700	720	986	1027	845	937	889	1026	1052	1183
P (BKN)	3·96	3·88	4·04	4·04	4·26	3·86	4·25	4·09	4·05	4·08
P (KB)	3·34	1·52	4·78	3·89	5·03	4·00	7·18		3·29	0·45
P (NG)	4·20	4·12	4·29	4·26	4·35	4·02	4·32	4·20	4·15	4·16
P (MC)	4·41	4·36	4·48	4·46	4·55	4·24	4·50	4·42	4·40	4·38
Thermobarometer combinations (solved iteratively) T *(°C)*, P *(GPa)*										
T (BKN/BKN)			1062	1011	925	955	772		1075	1221
P (BKN/BKN)			4·39	4·11	3·75	3·57	2·72		4·56	5·56
T (BKN/KB)			1091	1010	929	951	789		1067	1155
P (KB/BKN)			6·11	4·03	3·99	3·32	3·72		4·18	2·74
T (Krogh/BKN)			1049	1210	1022	1043	1449		1074	1199
P (BKN/Krogh)			4·32	5·24	4·41	4·13	7·25		4·56	5·42
T (O'Neill/BKN)	820	831	1062	1117	855	900	852		1053	1120
P (BKN/O'Neill)	2·84	2·84	4·39	4·71	3·28	3·22	3·26		4·41	4·89
T (Harley/BKN)	871	887	1035	1084	895	913	907		953	977
P (BKN/Harley)	3·15	3·19	4·24	4·52	3·55	3·30	3·63		3·73	3·93
T (OpxBK/BKN)	803	801	937	946	845	884	846		1031	1031
P (BKN/OpxBK)	2·73	2·66	3·67	3·74	3·21	3·11	3·22		4·27	4·29

References: BKN, Brey & Köhler (1990); KB, Köhler & Brey (1990); Krogh, Krogh (1988); O'Neill, O'Neill & Wood (1979) and O'Neill (1980); Harley, Harley (1984); EG, Ellis & Green (1979); Pow, Powell (1985); Wells, Wells (1977); BM, Bertrand & Mercier (1985); OW, O'Neill & Wall (1987); Bal, Ballhaus et al. (1991a, 1991b); WS, Witt-Eickschen & Seck (1991); NG, Nickel & Green (1985); MC, MacGregor (1974).

of LREE and HREE over MREE; (2) patterns with maxima at La–Ce and $La/Lu_N > 1$. The first pattern is more common, but the second occurs within the same sample and even within the rim of the same opx grain (e.g. in K17). Both opx patterns are depleted in all REE relative to chondrite, particularly in HREE (<0·05). Sm/Nd_N varies between 0·5 in opx with $LREE_N$ maxima between La and Nd, and is up to 1·4 in opx with a REE_N maximum at Sm (Fig. 4a, Table 3). Interestingly, those opx with super-chondritic Sm/Nd_N also have positive Hf anomalies (Fig. 5a). All opx show a strong positive Nb–Ta anomaly and a negative Y anomaly, and variable positive and negative Zr, Hf and Ti anomalies (Fig. 5a).

Clinopyroxene

Cpx porphyroblasts usually have homogeneous cores, with Type I samples having the highest and Type II the lowest Mg-number (93–96 and 87–92, respectively; Electronic Appendix Table A).

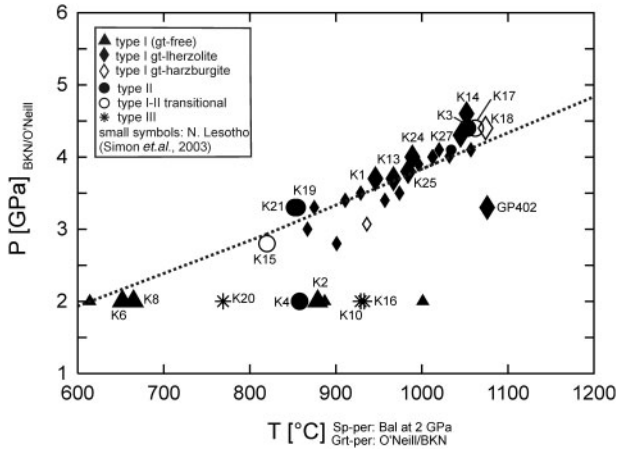

Fig. 3. *P–T* diagram showing the results of iterative pressure–temperature calculations for Kimberley and Lesotho xenoliths using *T*(O'Neill) and *P*(BKN) (Table 5 and Simon *et al.*, 2003). Temperatures for garnet-free peridotites are calculated with *T*ol–sp(Bal) at a fixed pressure of 2 GPa. Also shown for comparison is an average geotherm (dotted line) for the Kalahari craton derived by Rudnick & Nyblade (1999) from a wide range of xenolith *P–T* data from the Kaapvaal and Zimbabwe cratons.

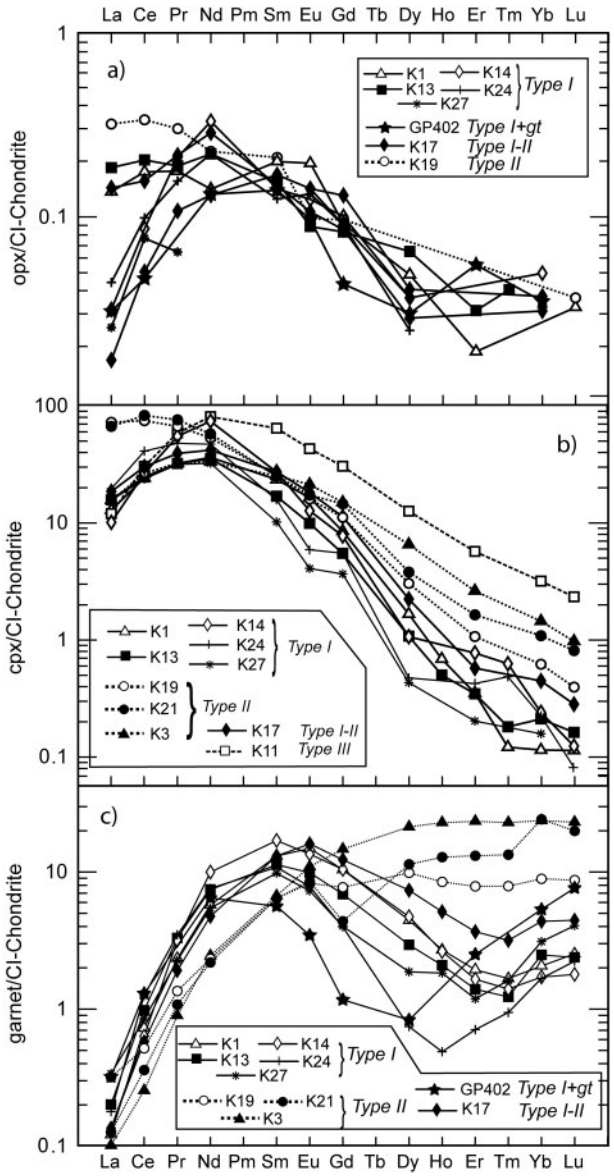

Fig. 4. Cl chondrite-normalized (McDonough & Sun, 1995) REE patterns of Kimberley minerals. (a) opx; (b) cpx; (c) garnet.

All cpx are significantly LREE enriched (Table 3, Fig. 4b, $La_N = 10–80$) and HREE depleted, leading to subchondritic Sm/Nd ($Sm/Nd_N = 0·4–0·8$) and Lu/Hf ($Lu/Hf_N = 0–0·13$) ratios. The cpx REE patterns of Type I samples are similar, especially in LREE concentrations ($La_N = 10–20$), and have extremely low HREE ($Lu_N \sim 0·1$). They have humped patterns with maxima at Pr–Nd [(30–80) × Cl]. In contrast, Type II samples K19 and K21 have cpx with REE maxima at Ce ($Ce_N \sim 80$). They also have the highest LREE, Ba, Th and Nb–Ta and HREE concentrations of all cpx. Sr, Zr and Hf concentrations are superchondritic in all cpx (Fig. 5b). All cpx have negative HFSE anomalies, but Type II and III samples have higher Zr–Hf and Ti contents.

Garnet

Mg-number in garnets (80·4–87·8, mean = 84) correlate positively with Cr-number (6·4–15·5, mean = 12). The lowest Cr_2O_3 (<3·1 wt% Cr_2O_3), highest Al (>21·5 wt% Al_2O_3) and relatively low CaO contents in garnet (<4·6 wt%) are found in Type II samples K3, K19 and K21 (and GP402), consistent with their differing textures and pyroxene major element chemistry (Electronic Appendix Table A). Only K3 (Type II) and K18 (Type I, deformed, high Cr-number and Mg-number) contain garnets with a significant amount of TiO_2 and Na_2O (0·3–0·4 wt% and 0·05–0·06 wt%, respectively). Garnets from GP402 and K15 are the only ones from Kimberley that have below 4·2 wt% CaO. All others have clearly lherzolitic Ca–Cr relations (Sobolev *et al.*, 1973). No significant zonation in major elements was observed in Kimberley garnets, with the exception of deformed sample K18.

Type I garnets have REE patterns that increase markedly from La to Nd ($La/Nd_N \sim 0·05–0·015$, Fig. 4c). The patterns are characterized by a maximum between Nd and Eu [(6·5–18) × Cl], a decrease in concentrations from Eu to Dy–Tm and $Dy–Tm/Lu_N < 1$, resulting in sinusoidal REE patterns (Table 3, Fig. 4c). Type II display very distinct LREE-depleted ($La_N = 0·1–0·3$) and HREE-enriched patterns ($Nd/Lu_N \sim 0·2–0·08$).

Garnet incompatible element patterns normalized to chondrite have low Ba and Sr, but high Hf and

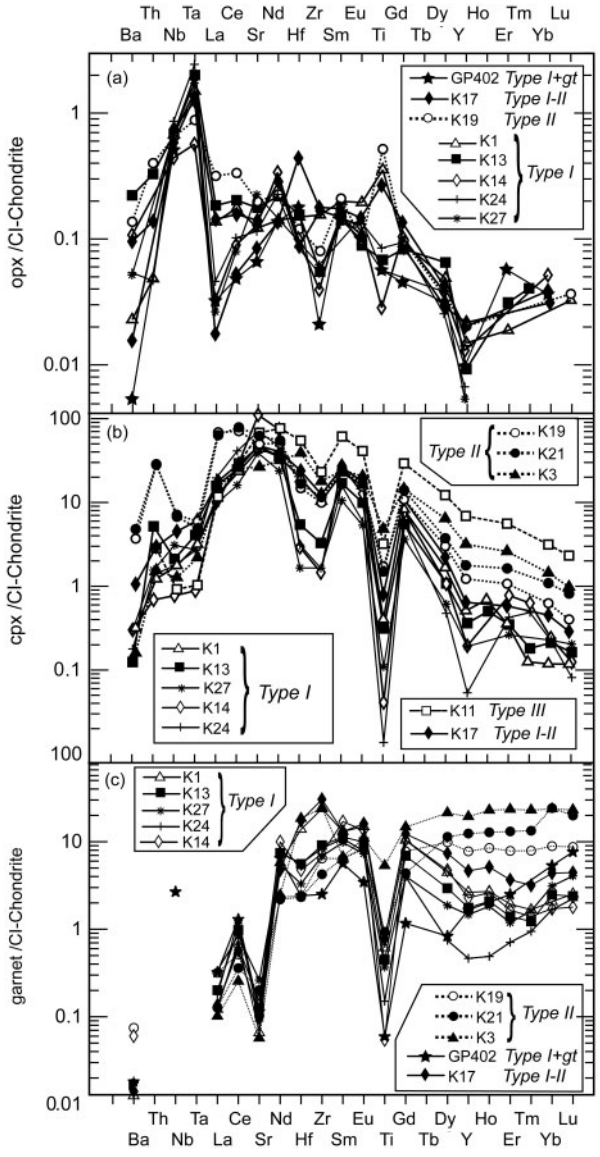

Fig. 5. Cl chondrite-normalized (McDonough & Sun, 1995) extended trace element diagram for Kimberley minerals. (a) opx; (b) cpx; (c) garnet.

Zr (Fig. 5c). Type I and Type I–II garnets have strong negative Ti anomalies, whereas the anomaly is less pronounced in Type II garnets. All garnets except K1, K3 and K17 have negative Hf–Zr (and Ti) anomalies and Zr and Hf concentrations similar to, or lower than, a primitive mantle garnet (Simon, 2004). All samples except GP402 ($Sm/Nd_N = 0{\cdot}85$) have superchondritic Sm/Nd ratios. Type I garnets (except GP402gt: $Lu/Hf_N = 2{\cdot}7$) have $Lu/Hf_N \ll 1$, whereas Type II garnets (and GP402gt) have $(Lu/Hf)_N > 1$.

Spinel

Primary spinels are magnesiochromites (Mg-number = 40–65, Cr-number ~ 50) with homogeneous compositions and very low Ti contents (Electronic Appendix Table A). Primary spinels coexisting with garnet are generally more Cr-rich (e.g. Boyd & Nixon, 1975; Boyd *et al.*, 1999).

Phlogopite and amphibole

Primary, texturally equilibrated phlogopite porphyroblasts have Mg-number varying from 93 to 95. TiO_2 contents vary from 0·05 to 1·7 wt% (Electronic Appendix Table A).

Amphiboles are K-richterites with variable major element compositions (Electronic Appendix Table A). Mg-number varies from 87 to 95. TiO_2 varies from 0 to 1·35, K_2O from 0·35 to 4·6 and Na_2O from 2·9 to 5·2 wt%. Amphibole was analysed for trace elements in Type III sample K11 (Table 3). The amphibole is LREE enriched ($La_N = 16$) with $La/Lu_N \sim 40$, has a small positive Eu anomaly, is strongly enriched in Rb relative to Ba and Th ($Rb_N = 300$, $Rb/Th_N \sim 100$) and has positive Sr and HFSE anomalies, and $Hf_N > Zr_N$ and $Nb_N > Ta_N$. K11 amphibole has subchondritic Sm/Nd_N and Lu/Hf_N ratios (0·56 and 0·02, respectively), but a high Rb/Sr ratio compared with primitive mantle ($Rb/Sr_{PM} = 7{\cdot}2$).

Whole-rock compositions of the xenoliths

Major and minor elements

Type I xenoliths are extremely depleted in magmaphile elements (Ca, Al, Na, Ti) and have high MgO contents and therefore Mg-number (Table 2). FeO contents are generally lower than in oceanic peridotites at a given Ca or Al, but typical for Kaapvaal low-T peridotites (e.g. Boyd, 1989). They are also characterized by low Mg/Si ratios, placing the Kimberley samples well above the oceanic trend of Boyd (1989; Fig. 6a). Type I and III samples have Cr_2O_3 contents within the range 0·20–0·44 wt%, with the garnet-bearing Type I samples having slightly higher Cr_2O_3 than the Type I spinel peridotites. Type II samples are variably enriched in CaO and/or Al_2O_3 (Fig. 6b), have the highest Cr_2O_3 (up to 0·6 wt%), and also tend to have lower Mg-number in olivine. In all samples, Cr_2O_3 increases with Al_2O_3 and decreases with MgO.

Although minor element contents might be affected by kimberlite contamination, most samples have very low TiO_2 and Na_2O contents (below 0·03 and 0·1 wt%, respectively). Elevated TiO_2 and Na_2O contents (up to 0·3 wt%) are found only in some Type II and III samples.

Trace elements

Measured whole-rocks show steep primitive mantle normalized ($_{PM}$) incompatible element patterns. They exhibit strong enrichment in the most incompatible elements with a maximum at Ba_{PM} of 9, $Ba/Lu \sim 10$, Lu_{PM} 0·1–1 and positive Nb and negative Hf and Ti anomalies (Table 6, Fig. 7). Whole-rock trace element contents reconstructed from mineral compositions and modes (Fig. 8) show markedly lower incompatible element

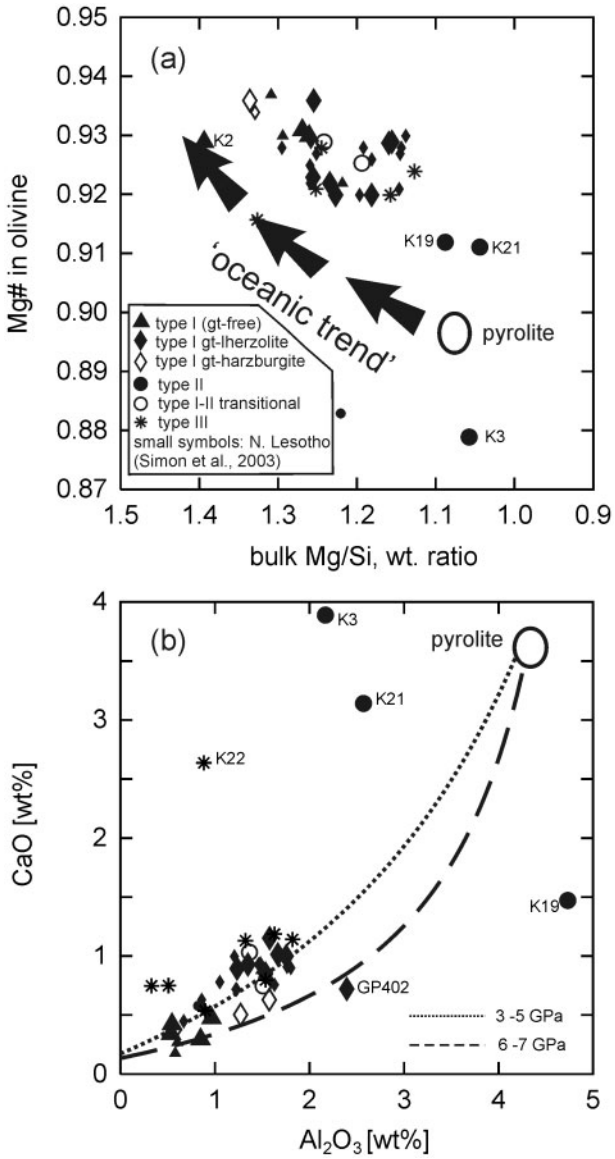

Fig. 6. (a) Mg-number in olivine vs Mg/Si wt% ratio in bulk-rocks. Oceanic trend from Boyd (1989). (b) CaO vs Al_2O_3 in whole-rocks. Black dashed and dotted lines are melting trends extrapolated from compositions of residua of melting experiments at 3–7 GPa from Walter (1998). Large open circle indicates pyrolite compositions (Ringwood, 1975).

concentrations and very distinct patterns compared with the measured whole-rock values, which reflects contamination of the xenolith by the extremely incompatible element-rich host magma (Hawkesworth *et al.*, 1983; Boyd & Mertzman, 1987; Schmidberger & Francis, 2001; Pearson & Nowell, 2002; Grégoire *et al.*, 2003). These reconstructed patterns do not include phlogopite and amphibole, because the modal abundance of these phases cannot be estimated accurately from either thin section or whole-rock major element concentrations. In addition, it is assumed that the incompatible trace element concentration of olivine is zero, because for many of these elements, the concentration was below detection by the analytical means employed. The lack of inclusion of phlogopite and amphibole may explain the large troughs in Ti concentration in the reconstructed patterns, and deficiencies in other HFSE such as Nb and Ta. The 30–180 ppm Ti concentrations measured in olivine would result in less than a doubling of the calculated whole-rock Ti concentration if included, and thus would not significantly erase the large Ti troughs observed in the reconstructed whole-rock patterns (Fig. 8). For other incompatible trace elements, olivine analyses by ion-probe showed abundances below detection limits, which implies that the contribution of olivine to the whole-rock abundances of these elements is minimal.

The reconstructed REE concentrations show several distinct patterns that are not always coherent with the classification derived from petrography and major element chemistry (Fig. 8). Most Type I whole-rock REE patterns are sinusoidal in shape, similar to the REE patterns of the garnets in these samples. Even though all samples show variable enrichment of MREE over HREE, all Type I rocks possess a positive slope in their HREE patterns ($Lu_N > Er_N$). K21 is most enriched in LREE ($Ce_N = 10$). K3 has a REE pattern similar to those displayed by cpx. This reflects the dominance of this mineral in the bulk-rock trace element budget in these rocks. K21 and K3 are the only samples that are enriched in trace elements relative to primitive mantle (Hofmann, 1988).

Re–Os, Sm–Nd and Lu–Hf isotopes

Whole-rock Re–Os isotope systematics

$^{187}Os/^{188}Os$ in the Kimberley peridotites range from 0·1073 to 0·1189 (Table 7), which overlaps values reported previously for Kimberley (Carlson *et al.*, 1999; Griffin *et al.*, 2004). Type I samples generally have low kimberlite eruption age-corrected $^{187}Os/^{188}Os$ (maximum 0·1106, average 0·1086), translating into Archaean T_{RD} model ages (Fig. 9) with a mean T_{RD} of $2{\cdot}80 \pm 0{\cdot}13$ Ga [Re-depletion ages as defined by Walker *et al.* (1989)]. Conventional Re–Os model ages (T_{MA}) show some scatter (Fig. 9; Table 7), mainly as a result of Re addition during entrainment of the xenoliths in the kimberlite (Simon *et al.*, 2003). However, the median T_{MA} (mantle model age) of 3·1 Ga approaches the 3·2 Ga age of the oldest basement rocks in the western Kaapvaal (Schmitz *et al.*, 2004). Some samples from the metasomatized Types II and III also have Archaean T_{RD} model ages, but others have younger ages, the youngest being 1·7 and 1·9 Ga (Table 7). These samples, in general, also have higher Re contents (Table 7).

Table 6: Whole-rock trace element contents (ppm) as measured by ICP-MS and reconstructed from mineral trace elements and modes

Type:	I (sp)	I (sp)	I (gt)	I (gt)	I (gt)	I (gt)	I (gt)	I (gt)	I (gt)	I (gt)	I (gt)	I (gt)	I (gt)	I (gt)	I–II	I–II	II	II	II	II	II	III
Sample:	K2	K6	K1	K1	K13	K13	K14	K18	K24	K24	K27	K27	GP402	GP402	K17	K17	K3	K3	K19	K19	K21	K11
	meas	meas	meas	calc	meas	calc	calc	meas	meas	calc	meas	calc	meas	calc	meas	calc	meas	calc	meas	calc	calc	calc
Li	0·80	0·84	0·91		1·11			0·90	1·06		0·97		0·78		1·18		1·36		1·60			
Be	0·03	0·01	0·08		0·09			0·14	0·06		0·05		0·04		0·08		0·30		0·13			
Sc	3·67	4·89	7·59		7·02			7·15	7·16		8·05		7·94		7·03		12·57		20·5			
Ti	41·0	7·3	121	88	95	40	5·0	374·4	73	36	86	37	15	11	145	81	308	756	280	208	302	473
V	13	20	32		27			22	30		33		26		27		70		37			
Co	103	95	91		98			94	100		94		84		95		89		87			
Cu	3·09	1·04	1·86		4·76			2·38	1·71		4·94		2·61		1·50		2·78		4·70			
Zn	43	42	191		51			45	47		45		40		48		46		45			
Ga	0·22	0·25	0·63		0·76			0·50	0·63		0·83		0·60		0·55		1·51		1·54			
Rb	1·02	0·60	6·10	0·08	1·24	0·04	0·10	7·59	1·37	0·04	1·36	0·10	1·66	0·12	1·20		2·58		4·15	0·13		0·01
Sr	27	22	26	9	34	8	17	21	33	12	29	11	27	0·20	21	5	115	37	35	8	58	15
Y	0·34	0·11	0·66	0·34	0·49	0·17	0·22	1·28	0·35	0·06	0·39	0·17	0·38	0·27	0·78	0·57	2·24	1·37	3·52	2·60	2·22	0·31
Zr	3·51	0·70	13·23	8·1	7·20	2·3	1·8	11·3	7·49	2·6	6·18	2·0	2·33	1·0	13·49	9·5	19·02	15	11·78	6·1	7·1	2·6
Nb	2·49	1·07	2·64	0·07	2·82	0·06	0·03	2·39	2·97	0·05	2·41	0·06	3·08	0·10	2·53	0·05	4·13	0·06	3·04	0·08	0·20	0·01
Mo	1·45	1·15	0·73		1·42			1·14	1·00		1·05		2·56		1·61		0·32		0·46			
Sn	0·08	0·03	0·11		1·41			0·09	0·43		0·05		0·02		0·07		0·21		0·09			
Cs	0·09	0·16	0·28		0·19			0·13	0·16		0·07		0·08		0·11		0·17		0·31			
Ba	14	11	15	0·04	28	0·16	0·09	19·09	24	0·04	14	0·07	26	0·01	15	0·05	46	0·07	28			
La	2·26	1·01	2·17	0·09	2·30	0·09	0·06	1·85	2·52	0·11	2·03	0·11	2·21	0·01	1·69	0·06	5·93	0·70	2·89	0·39	1·9	0·08

(continued)

Table 6: Continued

Type:	I (sp)	I (sp)	I (gt)	I (gt)	I (gt)	I (gt)	I (gt)	I (gt)	I (gt)	I (gt)	I (gt)	I (gt)	I (gt)	I (gt)	I–II	I–II	II	II	II	II	II	III
Sample:	K2	K6	K1	K1	K13	K13	K14	K18	K24	K24	K27	K27	GP402	GP402	K17	K17	K3	K3	K19	K19	K21	K11
	meas	meas	meas	calc	meas	calc	calc	meas	meas	calc	meas	calc	meas	calc	meas	calc	meas	calc	meas	calc	calc	calc
Ce	4·58	1·91	4·50	0·44	4·34	0·39	0·39	3·48	5·13	0·66	4·25	0·46	4·35	0·09	3·59	0·29	15	3·1	5·81	1·08	6·2	0·53
Pr	0·53	0·21	0·53	0·10	0·51	0·09	0·13	0·40	0·61	0·13	0·52	0·10	0·53		0·44	0·07	2·08	0·57	0·67	0·16	0·87	0·15
Nd	1·97	0·73	2·18	0·63	2·06	0·56	1·03	1·53	2·47	0·78	2·17	0·61	2·20	0·32	1·83	0·44	8·31	2·86	2·62	0·76	3·31	1·05
Sm	0·28	0·10	0·44	0·24	0·36	0·15	0·24	0·32	0·41	0·18	0·34	0·14	0·31	0·09	0·38	0·21	1·22	0·72	0·53	0·29	0·55	0·27
Eu	0·08	0·02	0·14	0·09	0·11	0·05	0·06	0·11	0·09	0·04	0·09	0·04	0·07	0·02	0·12	0·08	0·31	0·23	0·18	0·12	0·17	0·07
Gd	0·176	0·041	0·340	0·205	0·233	0·106	0·158	0·306	0·202	0·088	0·194	0·079	0·129	0·026	0·334	0·220	0·717	0·601	0·562	0·374	0·437	0·172
Dy	0·065	0·015	0·161	0·097	0·101	0·051	0·075	0·237	0·074	0·018	0·084	0·038	0·036	0·023	0·166	0·145	0·422	0·376	0·600	0·524	0·383	0·088
Ho				0·012		0·007	0·008			0·002		0·007			0·021	0·018		0·097	0·067			
Er	0·027	0·009	0·046	0·026	0·037	0·015	0·018	0·104	0·027	0·010	0·032	0·014	0·044	0·044	0·061	0·045	0·218	0·132	0·359	0·267	0·234	0·026
Tm	0·003	0·000	0·004	0·003	0·004	0·002	0·002	0·014	0·003	0·002	0·005	0·003	0·009		0·007	0·006	0·031	0·008	0·049	0·041	0·032	
Yb	0·016	0·007	0·033	0·026	0·029	0·024	0·019	0·077	0·030	0·021	0·029	0·036	0·085	0·090	0·046	0·055	0·213	0·097	0·346	0·303	0·396	0·015
Lu	0·002	0·001	0·005	0·005	0·005	0·005	0·003	0·011	0·005	0·004	0·005	0·007	0·018	0·020	0·009	0·008	0·033	0·013	0·053	0·045	0·050	0·002
Hf	0·070	0·012	0·264	0·164	0·137	0·049	0·037	0·219	0·148	0·052	0·117	0·030	0·045	0·030	0·251	0·181	0·444	0·812	0·182	0·088	0·241	0·168
Ta	0·088	0·026	0·142	0·008	0·132	0·009	0·002	0·106	0·146	0·008	0·126	0·008	0·177		0·133	0·006	0·177	0·006	0·130	0·005	0·008	0·000
Pb	0·456	0·257	1·635	0·025	0·411	0·016		0·346	0·310	0·026	0·277	0·026	0·297		0·203	0·009	1·092	0·068	0·810	0·078	0·301	0·018
Th	0·244	0·147	0·274	0·001	0·253	0·006		0·184	0·299	0·001	0·266	0·001	0·249		0·221	0·001	0·582	0·008	0·400	0·021	0·105	0·002
U	0·069	0·044	0·075	0·001	0·097	0·002	0·001	0·135	0·087	0·001	0·077	0·000	0·092		0·070	0·000	0·105	0·017	0·208	0·003	0·011	0·001
Cr	1140	2093	2648	3028	2526	3046	2660	2531	2206	2589	2588	3003	2368	2697	2309	3289	3570	1617	3871	4324	2939	4688
Ni	2179	2074	1851		2013			1943	2061		1869		1672		1976		1666		1504			

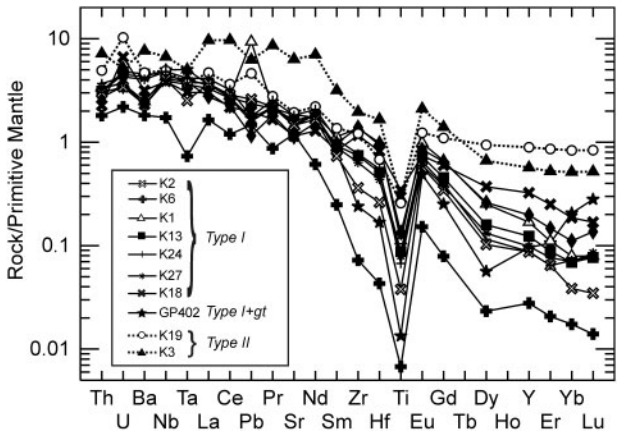

Fig. 7. Trace element compositions of Kimberley whole-rocks, normalized to primitive mantle values (Hofmann, 1988). Data obtained by ICP-MS on solutions of powdered whole-rocks.

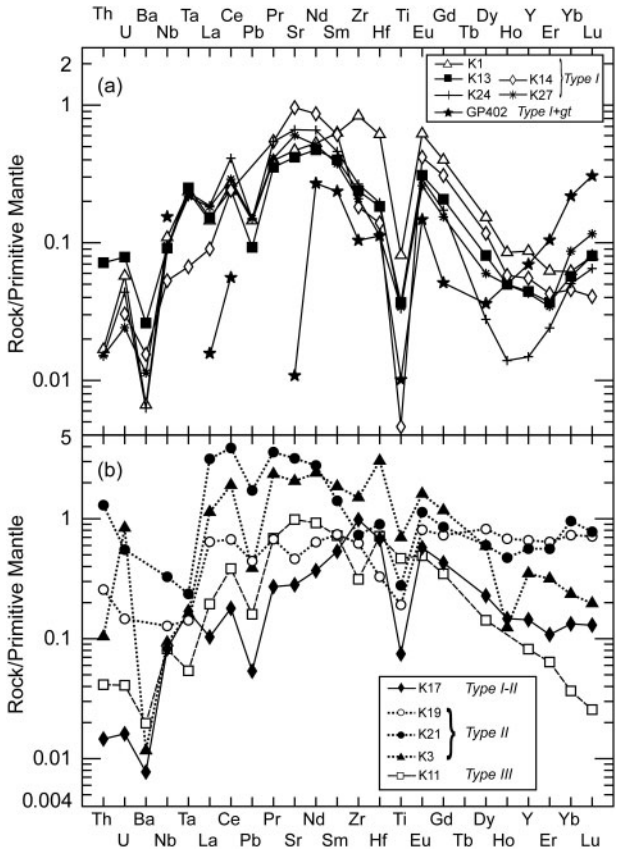

Fig. 8. Reconstructed whole-rock trace element compositions normalized to primitive mantle values. (a) Type I samples; (b) Transitional Type I–II, Type II and III samples.

Garnet and cpx Sm–Nd and Lu–Hf isotope systematics

Kimberley garnets and cpx have Nd isotope compositions (ε_{Nd} ranges from −13·5 to 0·3 with a median of −4·0; Table 4, Fig. 10) generally lower than, but overlapping the low ε_{Nd} end of the range displayed by South African Group I kimberlites (Smith, 1983; Nowell *et al.*, 2004). All Kimberley cpx have substantially subchondritic Sm/Nd (mean $^{147}Sm/^{144}Nd = 0{\cdot}095$), whereas the garnets show a range in $^{147}Sm/^{144}Nd$, but mostly superchondritic values (0·137–0·574, mean 0·353). The large difference in Sm/Nd, but the relatively similar Nd isotope compositions of the garnet and cpx from the same sample result in generally young two-point cpx–garnet Sm–Nd 'ages' for the Kimberley samples ranging from negative to 202 Ma (Table 8). Compared with the Kimberley samples, garnets from well-characterized Type I xenoliths from northern Lesotho (Simon *et al.*, 2003) generally show much lower Sm/Nd ratios. Nd isotope compositions for the Lesotho cpx cluster in a relatively narrow range just slightly more radiogenic than those from Kimberley (ε_{Nd} from −3·1 to 2·3, mean = 0·4) and fall completely within the field displayed by South African Group I kimberlites (Smith, 1983; Nowell *et al.*, 2004; Fig. 10). The Lesotho cpx Nd isotope compositions show no systematic variation with Sm/Nd ratio or Nd contents. In contrast, Lesotho garnets span a wide range in Nd isotope compositions (ε_{Nd} from −36·2 to 2·4, mean = −7·9), but are generally below chondritic (Fig. 10). Four out of seven of the Lesotho garnet–cpx isochrons provide negative 'ages' (Table 8).

In comparison with the generally subchondritic Nd isotope compositions, the Kimberley and Lesotho cpx and garnets tend towards superchondritic Hf isotope compositions (Table 4, Fig. 10). Lesotho garnets show a relatively restricted range in Hf isotope compositions with four out of five samples having ε_{Hf} between 12·8 and 22·8, well above the −6 to 7 range displayed by South African Group I kimberlites (Nowell *et al.*, 2004). Kimberley garnets show a much wider range in Hf isotope compositions (ε_{Hf} from −2·7 to 345, Fig. 10) that is accompanied by a wide range in Lu/Hf ratios. As a result, four of the Kimberley garnets provide depleted mantle Hf model ages between 0·87 and 1·04 Ga, whereas two samples provide Archaean ages (GP402: 2·85 Ga; K27: 3·3 Ga; Table 4). In contrast, three out of five Lesotho garnets provide Hf model ages that are either negative or near zero, whereas only one sample provides an old model age (M9: 1·73 Ga). Hf isotope compositions in cpx scatter within the range observed for South African Group I kimberlites (Nowell *et al.*, 2004), with similar median ε_{Hf} values of 6·6 for Kimberley and 3·7 for Lesotho.

DISCUSSION

The trace element and Nd–Hf systematics of the xenolith minerals clearly are not consistent with these samples being residua of a single stage of melt extraction. The incompatible element enrichment and low Nd and Hf isotope compositions of the cpx reflect the well-known propensity of CLM to have experienced metasomatic

Table 7: Re–Os isotope compositions of Kimberley whole-rocks

Type:	I				I								
	spinel harzburgites				(depleted) garnet harzburgites and lherzolites								
Sample:	K2	K6	K8	K9	K1	K13	K14	K24	K25	K27	K12	K18	GP402
Re (ppt)	22·6	11·4	31·6	52	36·9	9·5	32·8	8·1	84·3	15·7	32·2	32·1	23
Os (ppt)	282	1996	1420	3974	3006	2455	2396	4092	4452	4125	3901	1823	135
$^{187}Re/^{188}Os$	0·3842	0·0275	0·107	0·0629	0·059	0·0186	0·0658	0·0095	0·091	0·0183	0·0397	0·0846	0·8212
$^{187}Os/^{188}Os$	0·1111	0·1091	0·1081	0·1082	0·1096	0·1073	0·1085	0·1082	0·1092	0·1075	0·1085	0·1073	0·1118
2σ	0·00032	0·00145	0·00018	0·00017	0·000163	0·00012	0·00013	0·00011	0·00045	0·00015	0·00012	0·0003	0·00052
$^{187}Os/^{188}Os(i)$	0·1106	0·109	0·108	0·1081	0·1095	0·1073	0·1084	0·1082	0·1091	0·1075	0·10846	0·1072	0·1105
$\gamma Os(0)$	13·7	15·3	16	15·9	14·8	16·6	15·7	15·9	15·2	16·5	15·7	16·6	13·2
$\gamma Os(i)$	13·7	14·9	15·7	15·6	14·5	16·3	15·3	15·5	14·8	16·1	15·31	16·3	13·7
T_{RD} (Ga)	2·5	2·7	2·9	2·8	2·7	3·0	2·8	2·8	2·7	2·9	2·8	3·0	2·5
T_{MA} (Ga)	21·8	2·9	3·8	3·3	3·1	3·1	3·3	2·9	3·4	3·1	3·1	3·7	2·8
Type:	I–II		II			III							
	transitional		Ca–Al–Fe enriched			modal metasomatism (phl, am, oxides)							
Sample:	K15	K17	K3	K19	K21	K5	K7	K10	K11	K16	K20	K22	K23
Re (ppt)	214	32·3	37·4	85·1	61·2	194·8	73·7	50·4	29·2	22·8	171	46·2	45·2
Os (ppt)	2574	3706	2792	2619	180	790	2371	696	1746	1166	2327	1883	2009
$^{187}Re/^{188}Os$	0·3997	0·0419	0·0644	0·1563	1·634	1·1862	0·1494	0·3484	0·0804	0·094	0·3535	0·118	0·1082
$^{187}Os/^{188}Os$	0·1101	0·1114	0·1125	0·1152	0·1189	0·1126	0·1086	0·1085	0·1089	0·1091	0·1133	0·1126	0·1096
2σ	0·00014	0·00013	0·00014	0·00015	0·00048	0·00025	0·00012	0·00022	0·00014	0·00032	0·00013	0·00024	0·00017
$^{187}Os/^{188}Os(i)$	0·1095	0·1113	0·1124	0·1149	0·1165	0·1108	0·1084	0·108	0·1088	0·1089	0·1128	0·1124	0·1094
$\gamma Os(0)$	14·4	13·5	12·6	10·5	7·6	12·5	15·6	15·7	15·4	15·3	11·9	12·5	14·9
$\gamma Os(i)$	14·5	13·1	12·2	10·2	9	13·4	15·4	15·7	15	14·9	11·9	12·2	14·6
T_{RD} (Ga)	2·7	2·4	2·3	1·9	1·7	2·5	2·8	2·9	2·8	2·7	2·2	2·3	2·7
T_{MA} (Ga)	34·6	2·7	2·7	3·0	0·6	1·4	4·3	14·5	3·4	3·5	12·2	3·1	3·6

γOs is the deviation from a chondritic reservoir composition (CHUR) at a given time i (here 90 Ma, the time of kimberlite eruption) in percent ($\gamma Os_i = [(^{187}Os/^{188}Os)_{sample}/(^{187}Os/^{188}Os)_{CHUR} - 1] \times 100$), with present-day $(^{187}Os/^{188}Os)_{CHUR} = 0{\cdot}1287$. Model ages are calculated relative to primitive upper mantle (PUM; value from Meisel et al., 2001). T_{RD} values assume that all Re was removed during melting (Re = 0).

JOURNAL OF PETROLOGY VOLUME 48 NUMBER 3 MARCH 2007

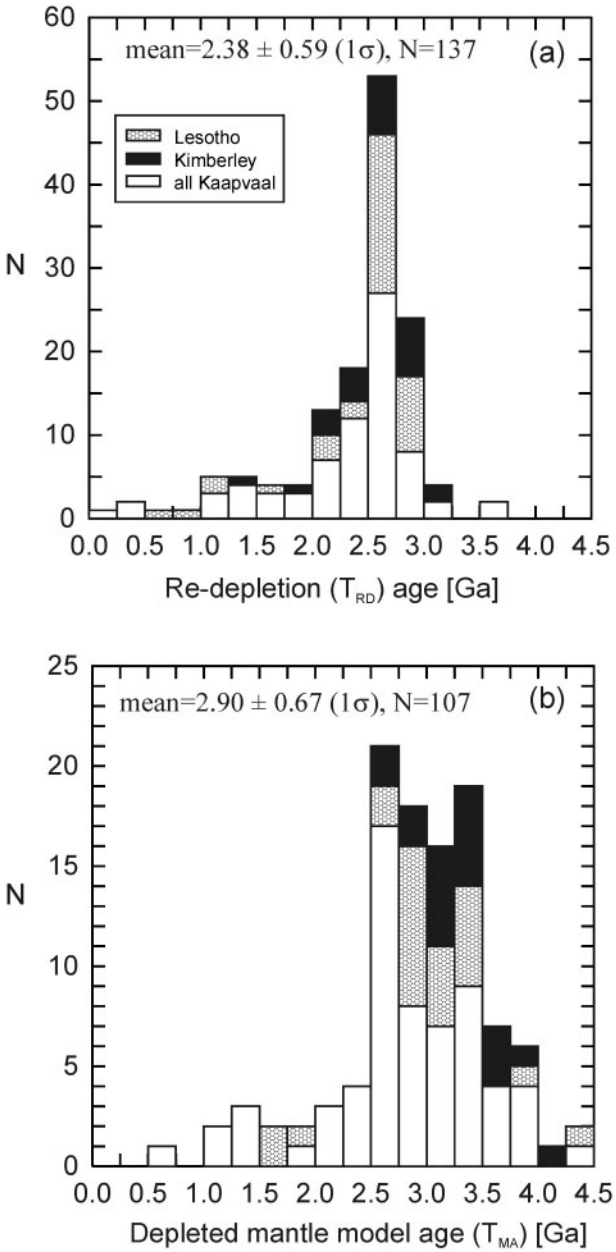

Fig. 9. Re–Os model age histograms. (a) T_{RD} Re-depletion ages (minimum ages); (b) depleted mantle model ages (T_{MA}). Lesotho data from Irivine *et al.* (2001) and Simon *et al.* (2003); Kaapvaal data from Walker *et al.* (1989), Pearson *et al.* (1995a), Carlson *et al.* (1999), Menzies *et al.* (1999) and Meisel *et al.* (2001); Kimberley data are from this study.

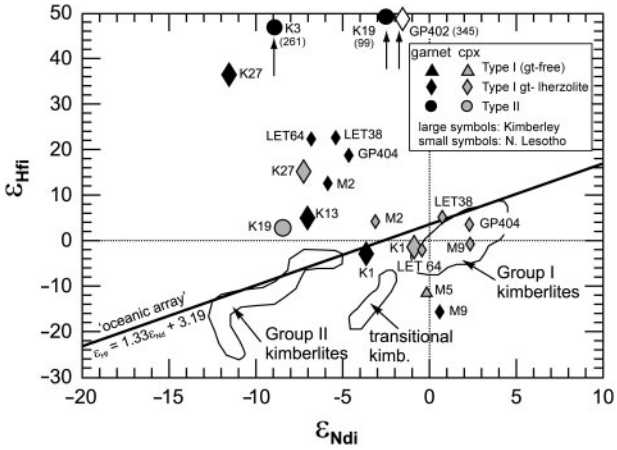

Fig. 10. ε_{Hfi} vs ε_{Ndi} isotope diagram showing the data for garnets and cpx from xenoliths from Lesotho and Kimberley. The fields for Group I, Group II and transitional kimberlites are also shown (data from Nowell *et al.*, 2004). Oceanic mantle array (regression line through ocean island and mid-ocean ridge basalt data) from Vervoort & Blichert-Toft (1999). K27, K19 and K3 garnets plot outside the diagram in εHf_i (values in parentheses, Table 4).

enrichment in these elements (e.g. Menzies & Murthy, 1980; Hawkesworth *et al.*, 1983; Menzies & Hawkesworth, 1987; Griffin *et al.*, 1999*b*). To determine how the Kaapvaal CLM was initially formed it is necessary first to understand how subsequent metasomatic events modified the CLM composition. We therefore explore the temporal evolution of the CLM by progressively stripping away the effects of metasomatism to provide a better estimate of the composition of the material left from the initial melting event that created the residual nature of the CLM.

Numerous studies have documented evidence for multiple metasomatic events affecting cratonic lithosphere [see the review by Pearson *et al.* (2003); and specifically for the Kaapvaal the studies by Carlson *et al.* (1999) and Griffin *et al.* (1999a, 2004)]. The large-scale geological events recorded in the Kaapvaal craton that may have resulted in metasomatism in the CLM include: (1) major crust formation in the Palaeoarchaean (e.g. Eglington & Armstrong, 2004); (2) Mesoarchaean accretion of the western and eastern Kaapvaal blocks, accompanied by subduction of the eastern Kaapvaal underneath the western Kaapvaal block at 2·9 Ga (Drennan *et al.*, 1990; Schmitz *et al.*, 2004); (3) Ventersdorp magmatism at 2·7 Ga (e.g. Armstrong *et al.*, 1991); (4) accretion of the surrounding Proterozoic belts in the Mesoproterozoic (e.g. Hartnady *et al.*, 1985); (5) Karoo and/or Type II kimberlite magmatism at ~200–110 Ma (e.g. Hamilton *et al.*, 1998; Konzett *et al.*, 2000); (6) Group I kimberlite magmatism at 90 Ma (Allsopp & Barrett, 1975).

Interaction with kimberlite during entrainment and transport of the xenoliths

All xenoliths show evidence for infiltration of kimberlitic material [see petrography section and Simon *et al.* (2003)], as is reflected in the whole-rock trace element data, which show up to 10 times enrichment in incompatible elements relative to primitive mantle in comparison with the reconstructed whole-rock trace element patterns,

Table 8: Garnet–cpx tie-line ages (Ma)

Sample	Sm–Nd	Lu–Hf
K1	25 ± 6	−309 ± 200
K3		844 ± 9
K13		−28 ± 150
K17	88 ± 8	
K19	202 ± 5	825 ± 20
K21	78 ± 7	
K24	52 ± 9	
K27	−209 ± 9	755 ± 37
TP5	602 ± 120	
LET64	96661	588 ± 120
LET38	−344 ± 18	1995 ± 87
GP404	−171 ± 21	1026 ± 100
M2	−19 ± 6	659 ± 64
M9	91 ± 16	−2377 ± 130
M13	−2247 ± 120	

which are markedly incompatible element depleted for all Type I and III samples (Table 6, Figs 7 and 8). The discrepancy between measured and reconstructed trace element contents of CLM xenoliths has been known for some time (e.g. Hawkesworth *et al.*, 1983) and was most recently documented in cratonic mantle xenoliths from Siberia (Pearson & Nowell, 2002), Somerset Island (Schmidberger & Francis, 2001) and Kaapvaal (Pearson & Nowell, 2002; Grégoire *et al.*, 2003). For the Kimberley samples studied here, there is relatively good agreement between measured and reconstructed whole-rock compositions for moderately incompatible elements (D > Hf), whereas all the measured LREE, LILE and Nb and Ta contents are five (Nd) to several hundred times (Ba) higher than the recalculated concentrations (Table 6, Figs. 7 and 8). Simple mass-balance mixing calculations show that the difference between calculated and measured trace element concentrations can be accounted for by ~1·5% addition of an average Group I kimberlite for most elements, similar to estimates for Somerset Island (Schmidberger & Francis, 2001). The contribution of the kimberlite to the whole-rock budget for some of the highly incompatible elements (Ba, Rb, Th, Nb, Nd, Hf) can exceed 90% (e.g. Grégoire *et al.*, 2003) and thus control whole-rock Nd and Hf isotope compositions. In contrast, 1·5% addition of a kimberlite with 1 ppb Os (e.g. Carlson *et al.*, 1996) and $^{187}Os/^{188}Os = 0{\cdot}13$ to a residual peridotite with 3 ppb Os and $^{187}Os/^{188}Os = 0{\cdot}107$ would increase the measured whole-rock $^{187}Os/^{188}Os$ to only 0·1071, reducing the calculated Re-depletion age by only 10 Myr. Thus, kimberlite contamination is unlikely to have a significant effect on the whole-rock Re depletion ages measured for peridotite xenoliths.

Evidence for chemical disequilibrium between minerals within individual peridotites would provide unequivocal evidence that the peridotites had been modified by processes that occurred during or shortly before the entrainment by the host lavas. The mineral compositions of the Kimberley Type I samples provide temperature and pressure estimates using a variety of thermobarometers (Table 5) that plot along the 'Kalahari geotherm' determined for a wide variety of peridotite xenoliths from South Africa (e.g. Rudnick & Nyblade, 1999). This is suggestive of the attainment of major element chemical equilibrium between the phases while these rocks were resident at depth in the Kaapvaal CLM. Similarly, trace element partition coefficients between Kimberley garnet and cpx porphyroblast cores ($D^{gt/cpx}$) were calculated and compare well with equilibrium values (e.g. Zack *et al.*, 1997). In contrast to the results from the northern Lesotho xenoliths (Simon *et al.*, 2003), garnet and cpx in all Kimberley samples, except Type II samples K19 and K21, seem to be in trace element equilibrium. K19 and K21 (and to a lesser extent also K3), however, have $D^{gt/cpx}$ for LREE, MREE and HFSE that are about three times lower than reference equilibrium values, and also show a range in pressure and temperature estimates from different thermobarometers (Table 5). These features all suggest that the minerals within these Type II samples were not in equilibrium at the time they were brought to the surface.

Evidence that complete equilibration was not achieved in many of the samples comes from the observation that tie-lines connecting the garnet and cpx Sm–Nd data for seven samples (Table 8) provide ages younger than the time of kimberlite eruption (86 Ma: Allsopp & Barrett, 1975; Davis, 1977), including a number of samples that give negative ages. For example, K27 gives a negative Sm–Nd garnet–cpx age because the K27 garnet has markedly lower $^{143}Nd/^{144}Nd$ than the K27 cpx despite the higher Sm/Nd of the garnet. Negative Sm–Nd garnet–cpx ages are not uncommon for peridotite xenoliths (Günther & Jagoutz, 1991; Carlson *et al.*, 2004) and were first described in samples from Kimberley (Richardson *et al.*, 1985).

The Lu–Hf system has previously been shown to be more robust towards metasomatic processes and probably has a higher closure temperature than the Rb–Sr and Sm–Nd systems, particularly in garnet (Schmidberger *et al.*, 2002; Bedini *et al.*, 2004; Pearson & Nowell, 2004). Nevertheless, samples K1, K13 and M9 yield negative Lu–Hf garnet–cpx ages whereas the ages for the other seven garnet–cpx pairs range from 659 to 1995 Ma (Table 8). There is no clear correlation between equilibration temperature and Lu–Hf ages.

Indeed, the samples with the highest equilibration temperatures yield the highest garnet–cpx Lu–Hf isochron and garnet Hf depleted mantle model ages, which is the opposite of what would be expected if the age differences are due solely to cooling through a Lu–Hf closure temperature as suggested by Bedini *et al.* (2004). As with Nd, the Hf depleted mantle model ages for the majority (21 out of 24) of the cpx range from 0·5 to 1·5 Ga, overlapping the model ages of Group I kimberlites (Smith, 1983; Nowell *et al.*, 2004). This overlap, the negative garnet–cpx ages, the calculated trace element compositions of liquids that could be in equilibrium with the cpx in Lesotho xenoliths (Simon *et al.*, 2003), and the identification of trace element zonation in garnet grains in the Lesotho samples (Simon *et al.*, 2003), all suggest that the Nd–Hf systems in these minerals have been affected by recent chemical exchange with a metasomatic agent that had trace element and Nd–Hf isotope compositions similar to those of Group I kimberlites (Simon *et al.*, 2003; Simon, 2004) as has been suggested previously (Carswell, 1975; Shimizu, 1999; Van Achterbergh *et al.*, 2001; Grégoire *et al.*, 2002, 2003; Simon *et al.*, 2003).

Evidence for localized silicate melt metasomatism from Type II peridotites

Type II samples record some melt depletion in that they retain high Mg-numbers in olivine, but have been extensively modified by incompatible element addition and growth of new, metasomatic silicate phases such as cpx and garnet. This is evident from their major element variations compared with melt residua, their trace element concentrations and their petrographic appearance. K19 and K21 have garnet and cpx that are not in textural and chemical equilibrium with olivine and opx, which suggests that the metasomatic event occurred relatively close in time to kimberlite eruption. Type II sample K3 has a distinct texture, is much more Fe-rich and Mg-poor than all other samples, has a very high cpx content (19%) and contains minerals of the IRPS suite. This sample clearly has been extensively melt-modified and is suitable as an end-member for Fe + Ca addition to the lithosphere. Using the distribution coefficients given in Electronic Appendix Table B2, calculated melts in equilibrium with cpx and garnet in Type II samples K3, K19 and K21 have distinctively higher HREE and Ti contents than the Type I equilibrium melts (Fig. 11), indicating reaction with a silicate melt. The melts in equilibrium with Type II cpx have markedly higher incompatible element concentrations than the garnet melts (Fig. 11b), confirming chemical disequilibrium in these samples.

Type II samples also possess more radiogenic Os (but generally lower Os contents; Table 7) than Type I rocks, and their Os isotope compositions correlate positively with CaO and Al_2O_3 contents (Fig. 12). Types II and III, in general, have higher Re contents than the Type I samples (Table 7), consistent with Re addition during metasomatism. The Type II samples also are shifted away from the opx (SiO_2)–$^{187}Os/^{188}Os$ trend shown by Type I samples (Fig. 13), indicating a distinct metasomatic history for these samples. All of these characteristics suggest that the Type II samples were affected by interaction with mafic, instead of kimberlitic or carbonatitic, melts.

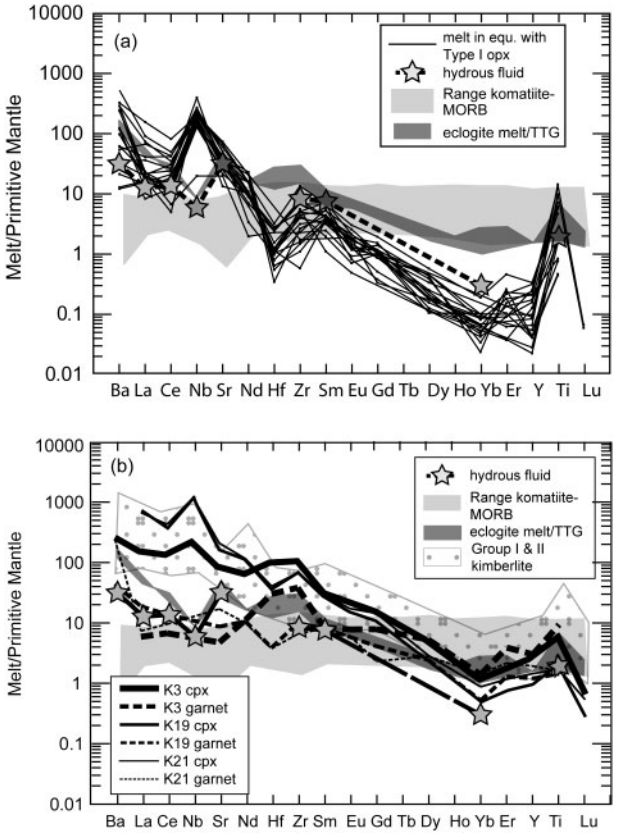

Fig. 11. Primitive mantle normalized trace element patterns for potential metasomatic agents and hypothetical melts that would be in equilibrium with (a) opx cores from Type I Kimberley and Lesotho xenoliths; (b) Type II garnets and cpx. Hypothetical melts in equilibrium with Type I garnets are not plotted, but overlap with those of the opx shown in (a). Hydrous fluid from experiments by Stalder *et al.* (1998); experimental partial melt of eclogite from Rapp *et al.* (1999); N-MORB from Hofmann (1988); Barberton komatiite from Lahaye *et al.* (1995); kimberlite from G. M. Nowell (unpublished data, 2004).

The origin of orthopyroxene introduction and garnet enrichment

To constrain the nature of possible metasomatic agents that led to incompatible element enrichment of the garnets and introduction of opx, we calculated the trace element compositions of hypothetical liquids in equilibrium with opx, garnet and cpx in the xenoliths. The range in published $D^{min/melt}$ values is large, especially for $D^{px/melt}$ (Electronic Appendix Table B2), but the major

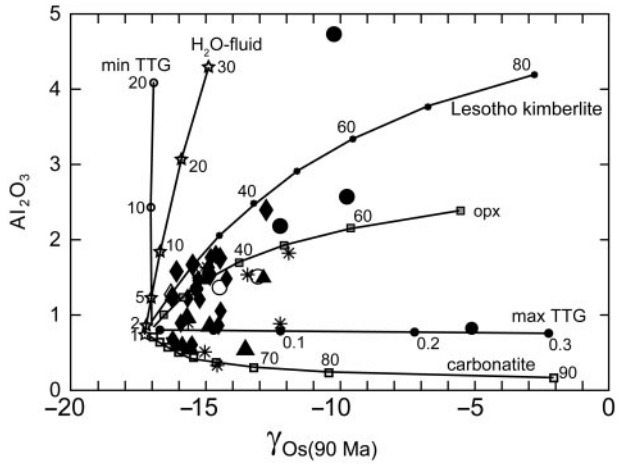

Fig. 12. $\gamma_{Os(90\ Ma)}$ vs whole-rock Al_2O_3 content (wt%) of the Kimberley xenoliths. The lines indicate mixing lines between a strongly depleted mantle end-member and various fluids and melts (compositions are listed in Electronic Appendix Table B1). Mixing is calculated at 90 Ma. Labels on the curves indicate amount of metasomatic component added in per cent. Symbols are as in Fig. 2.

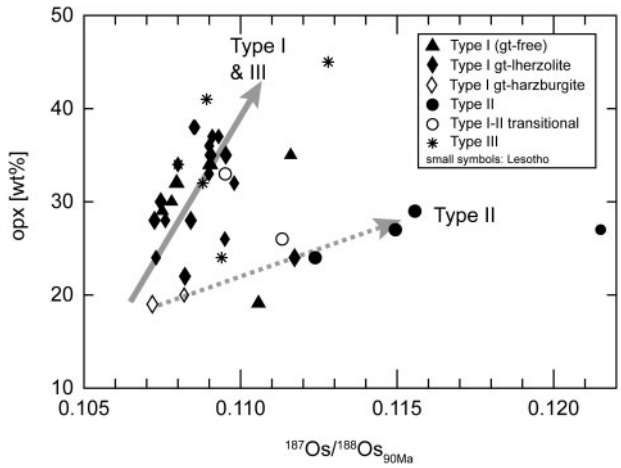

Fig. 13. Correlation of calculated modal orthopyroxene content with $^{187}Os/^{188}Os$ of the whole-rocks at 90 Ma.

consequence of this variation on the calculated patterns is to shift similar-shaped patterns up and down in Fig. 11. In most samples, the calculated liquids in equilibrium with opx (Fig. 11a) and garnet (not shown) are within error of one another. In the samples where opx cores and rims were analysed (e.g. K17, LET64), the less enriched cores overlap with the garnet liquid compositions, whereas the more LREE-enriched rims usually match the cpx equilibrium liquids (Simon, 2004). The liquids in equilibrium with garnet and opx (cores) display strong enrichment of Ba and LREE (La_{PM} up to >1000) over HREE ($Yb_{PM} = 0{\cdot}02$–$0{\cdot}3$), positive Nb and Ti, and negative Hf (and, less pronounced, Zr) anomalies (Fig. 11a). These characteristics are incompatible with equilibration with normal mafic melts. The high Ba, Nb and LREE might indicate re-equilibration with a kimberlitic melt, whereas MREE and HREE contents are too low to be in equilibrium with a Group I or II kimberlite. One alternative explanation is that a kimberlitic melt or fluid that percolates through a garnet-bearing peridotite will have its HREE preferentially removed by partial equilibration with garnet, leaving the residual fluid depleted in these elements through the process of chromatographic fractionation (Godard *et al.*, 1995). Another alternative notes that the LREE to HREE ratio of the hypothetical opx liquids fits remarkably well those of the hydrous fluid determined experimentally by Stalder *et al.* (1998) in equilibrium with eclogite-assemblage minerals (garnet, clinopyroxene, and rutile) at 900–1200°C and 3·0–5·7 GPa (Electronic Appendix Table B2). The positive Ti and negative Hf anomalies in the calculated liquids are pronounced, but also agree with the experimental fluid composition reported by Stalder *et al.* (1998). More recent experiments on hydrous mid-ocean ridge basalt (MORB) at 4 and 6 GPa and 700–1200°C, including a larger range of trace elements, yield similar fluid compositions, but also show that there is a continuous transition between aqueous fluids and hydrous silicate melts at these conditions (Kessel *et al.*, 2005). The fluids or melts of the experiments of Kessel *et al.* (2005) are characterized by a negative Y anomaly, a feature that is also shown by many of the opx from Lesotho (Simon *et al.*, 2003) and Kimberley (Fig. 5a) and the hypothetical melts that were calculated to be in equilibrium with those opx (Fig. 11a). The strongly positive Nb anomaly shown by the melts that would be in equilibrium with opx, however, can only be accounted for by the involvement of kimberlites.

If the LREE re-enrichment of the samples was due to an aqueous fluid, this fluid must also have enriched the CLM in other fluid-mobile elements such as LILE. Ti is assumed to be immobile in fluids, whereas the HFSE content of the fluid depends strongly on the presence or absence of HFSE-rich minerals, such as rutile, in the subducting slab (e.g. Stalder *et al.*, 1998; Foley *et al.*, 2000). The garnets in samples least affected by recent metasomatism (those with the lowest ε_{Nd}: K27, M13, LET2) tend to have high LREE, Rb and Sr, and low Hf (high Zr/Hf), Ti and HREE contents (and high LREE/HFSE and low HREE/HFSE ratios), relatively high Cr-number, low FeO, high Sm/Dy, high Nb and low whole-rock γOsi (−17 to <−14). The FeO and Ti contents in the garnets increase with decreasing LREE/HREE fractionation, hence the least LREE-enriched garnets have the highest Ti and FeO concentrations. Garnets also have less sinusoidal REE patterns (lower Sm/Dy) with increasing FeO and TiO_2 (Fig. 14)

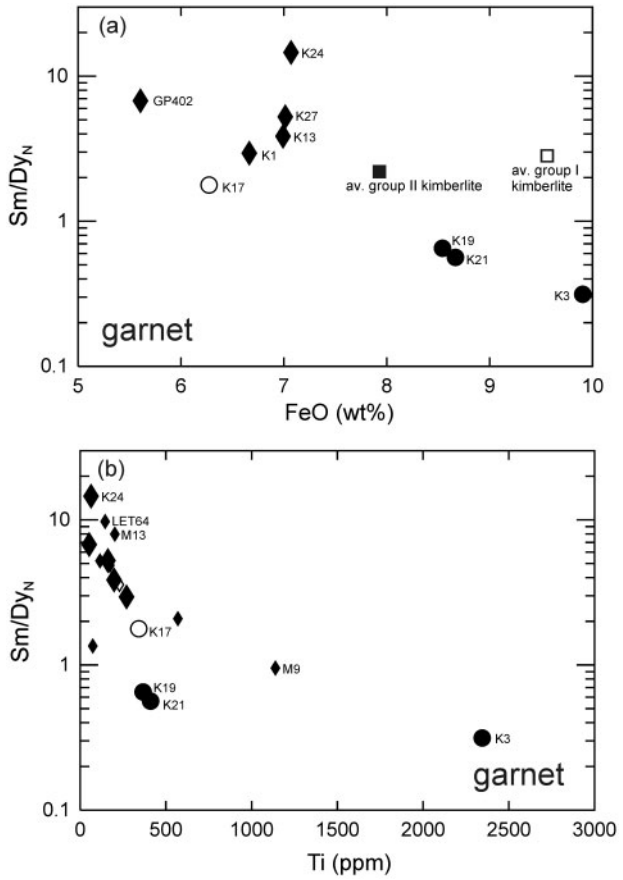

Fig. 14. Sm/Dy_N vs FeO (wt%) (a) and Ti (ppm) (b) contents in garnets. Also shown are the compositions of average Type I and II kimberlites (squares, Nowell *et al.*, 2004). Symbols are as in Fig. 6.

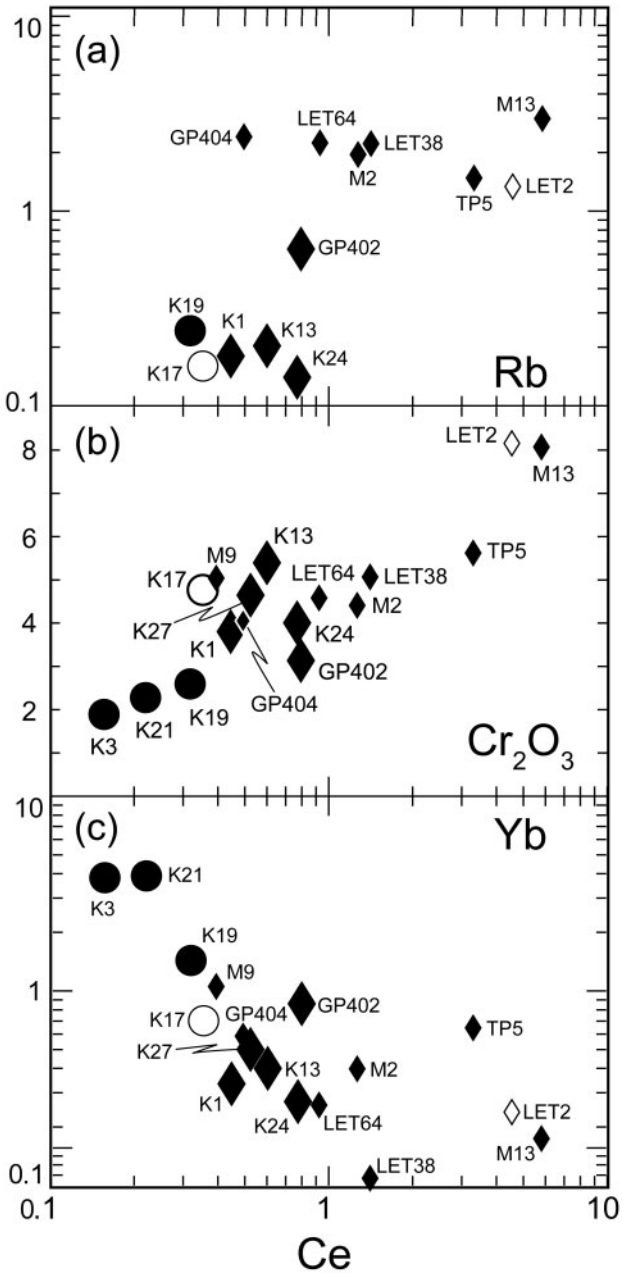

Fig. 15. Correlation of LREE (Ce) content in garnet with (a) Rb, (b) Cr_2O_3 (wt%) and (c) Yb. All but Cr_2O_3 in ppm. Symbols are as in Fig. 6.

and show positive correlations between LREE, LILE and Cr_2O_3, but a negative correlation between LREE and HREE (Fig. 15). Thus, it appears that the process that led to the LREE enrichment of garnets also leads to enrichment in LILE and a relative depletion in HFSE and possibly HREE. Ti, FeO and Cr_2O_3 contents in the garnets from Type I xenoliths are apparently not affected by this process, whereas Ti and FeO increase and Cr_2O_3 decreases in the garnets from samples that experienced metasomatism by a mafic or kimberlitic melt (most pronounced in Type II garnets). Similar characteristics (extreme depletion in HREE accompanied by enrichment in LREE relative to a residue of dry melting) have been described by Bizimis *et al.* (2000) for ophiolitic peridotites from the Hellenic Peninsula and were interpreted by those workers to reflect fluid-fluxed melting and simultaneous highly incompatible element enrichment in a supra-subduction zone setting.

The above chemical trends are consistent with previous findings by other workers (e.g. Pearson *et al.*, 1995*b*; Griffin *et al.*, 1999*b*; Shimizu *et al.*, 1999; Zhang *et al.*, 2003), but are interpreted differently here. Whereas previous studies related the LREE enrichment and sinusoidal REE patterns of garnets to metasomatism by carbonatitic melts (e.g. Pearson *et al.*, 1995*b*; Griffin *et al.*, 1999*b*), or the melts that formed the ilmenite–rutile–phlogopite–sulphide veins in the mantle (Zhang *et al.*, 2003), we support the suggestion that the observed geochemical characteristics are most consistent with metasomatism by a hydrous fluid (e.g. Bizimis *et al.*,

2000; Stachel *et al.*, 2004; Bell *et al.*, 2005). These fluids might have also caused some additional fluid-fluxed melting (e.g. Bizimis *et al.*, 2000), probably in Archaean subduction zones. This conclusion is supported by oxygen isotope data for garnets from polymict xenoliths. Zhang *et al.* (2003) found distinctly lower $\delta^{18}O$ (<5) in dark-coloured garnets with sinusoidal REE patterns than in light-coloured garnets with 'normal', HREE-enriched patterns, from the same samples. Peridotitic garnet inclusions in diamonds also show a relatively wide range of $\delta^{18}O$ (Lowry *et al.*, 1999) extending to lower values (4·5) than those typical for peridotite xenoliths ($\delta^{18}O = 5–5·5$; Mattey *et al.*, 1994), and Pearson *et al.* (2003) showed that low-Ca garnets in general have low $\delta^{18}O$. These lower than normal $\delta^{18}O$ values might indicate metasomatism of the sinusoidal garnets by slab-derived metasomatic agents, whereas the garnets with low $LREE/HREE_N$ were formed or overprinted by reaction with mantle-derived melts such as alkali basalts or kimberlites.

A slab-derived hydrous fluid was discussed as a potential source for crystallization of opx in the mantle wedge (Kesson & Ringwood, 1989; Smith *et al.*, 1999; Morishita *et al.*, 2003; Bell *et al.*, 2005) because in addition to the trace element characteristics discussed above it could be a carrier of Si and Mg into the mantle without addition of many other major elements (such as Al, Ca, Fe, etc.). Si and Mg have been shown experimentally to be soluble in a hydrous fluid under high pressures (Stalder *et al.*, 2001; Mibe *et al.*, 2002). In addition, hydrous fluids might be able to migrate over long distances through the mantle (Mibe *et al.*, 1998), making fluids more suitable agents for introduction of Si into the lithosphere than highly siliceous slab melts, because Si-rich melts from subducted crust are likely to react instantaneously with the surrounding mantle and form opx-rich layers at the interface between eclogite and peridotite (Yaxley & Green, 1998). Si-rich melts such as trondjhemites also have significant Al contents, and this led Carlson *et al.* (1999) to reject such granitoid melts as likely metasomatic agents (Fig. 12).

Timing of orthopyroxene introduction and ancient metasomatism

The spinel and garnet peridotites (Type I) and most phlogopite and phlogopite–amphibole peridotites (Type III) follow a steep trend of increasing $^{187}Os/^{188}Os_{90\,Ma}$ with increasing modal orthopyroxene (Fig. 13). The garnet and/or cpx-rich samples (Type II) show a shallower trend of moderately increasing orthopyroxene with rapidly increasing $^{187}Os/^{188}Os_{90\,Ma}$. The trends overlap at $^{187}Os/^{188}Os = 0·106$, which is equivalent to a T_{RD} of 3·2 Ga, the same age as the oldest crustal rocks in the western Kaapvaal. This convergence in isotopic composition suggests that the samples were modified from the same primary composition, an orthopyroxene-poor, olivine-rich harzburgite, and that the olivine-rich parental rock experienced melt extraction in the Palaeoarchaean. The trend of increasing $^{187}Os/^{188}Os_{90\,Ma}$ with increasing modal orthopyroxene (a proxy for SiO_2; Fig. 13) is not accompanied by increases in Re/Os (Table 7), suggesting that the increase in $^{187}Os/^{188}Os$ reflects the addition of radiogenic Os through interaction with the fluid or melt that deposited the opx. A key feature that constrains both the composition of the fluid or melt involved and possibly also the tectonic setting of its genesis is that the Type I samples do not show increasing CaO, TiO_2 or Re concentrations with increasing orthopyroxene and $^{187}Os/^{188}Os$. These features are similar to those displayed by modern xenoliths from subduction zones (Brandon *et al.*, 1996; Widom *et al.*, 2003), where the metasomatic agent appears to be an Os-rich hydrous fluid (e.g. Brandon *et al.*, 1996; McInnes *et al.*, 1999; Widom *et al.*, 2003; Becker *et al.*, 2004). The $^{187}Os/^{188}Os$ of the metasomatic agent in Type I samples is poorly constrained by the data, but the most radiogenic of these samples has a $^{187}Os/^{188}Os$ of 0·1105, compared with a fertile mantle composition at 2·9 Ga of 0·108. An estimate of the Os isotope composition of subduction-derived fluids present beneath Kimberley at 2·9 Ga can be derived from the initial Os isotope composition of eclogite-paragenesis sulphides found in Kimberley diamonds of $^{187}Os/^{188}Os = 0·156$ (Richardson *et al.*, 2001). If the metasomatic agent for Type I samples had an Os isotope composition similar to the initial ratio of the diamond inclusion sulphides, then to raise the Os isotope composition of a 3·2 Ga residual peridotite with 3 ppb Os and $^{187}Os/^{188}Os$ of 0·1055 to $^{187}Os/^{188}Os = 0·1105$ would require fluid/rock ratios of 4 and 0·7 for fluid Os concentrations of 0·1 and 1 ppb, respectively.

The Os data do not tightly constrain the timing of the opx addition, but they are suggestive of a Palaeoarchaean protolith for the Kaapvaal CLM, in agreement with numerous previous studies (Walker *et al.*, 1989; Pearson *et al.*, 1995*a*; Carlson *et al.*, 1999; Carlson & Moore, 2004; Griffin *et al.*, 2004). We have made the argument above that the opx addition was associated with the addition of LREE and LILE, in which case the Sm–Nd and Lu–Hf systems should provide chronological information on this event. Unfortunately, extracting chronological information from the Nd and Hf data is compromised by the obvious evidence for recent interaction of the samples with highly incompatible element-rich melts discussed previously. The most compelling evidence for ancient metasomatism of the Kaapvaal CLM is provided by the very low $^{143}Nd/^{144}Nd$ and Palaeoarchaean model ages for diamond inclusion garnets from Finsch and Kimberley (Richardson *et al.*, 1984). Of the samples studied here, those that are considered to be least affected

by interaction with the kimberlite (K27, M13 and LET2) have garnets with $^{143}Nd/^{144}Nd$ approaching the low values measured for Kimberley diamond inclusion garnets, but the >4·5 Ga model ages of K27gt and M13gt indicate that even these samples have inconsistent Sm–Nd isotope relationships, probably reflecting later metasomatic events and re-equilibration with (late metasomatic) cpx. Of these three samples, in part because of the very low Hf contents of their garnets, we were able to obtain Hf isotope data only for K27, where a depleted mantle model age of 3·3 Ga was obtained. This age supports a Palaeoarchaean origin for this sample, as does the 2·85 Ga Hf model age of GP402 garnet, but these are the only two samples in the dataset that provide Archaean Hf model ages. An important observation for the K27 garnet data, however, is that, for a garnet, this sample has a relatively low Lu/Hf ratio, and hence its model age probably dates the time of LILE enrichment, not the original depletion event. For example, in comparison with the relatively low $^{176}Hf/^{177}Hf$ ($\varepsilon_{Hf} = 36·6$) measured for K27 garnet, a garnet in a Palaeoarchaean strongly melt-depleted residue would have ε_{Hf} of many tens of thousands (Simon, 2004).

Depth and extent of the initial melting of the protolith

Provided that the effects of metasomatic mineral formation and compositional modification can be adequately accounted for, it is possible to constrain the original partial melting environment of the Kaapvaal mantle using the major and trace element systematics of the CLM peridotites. The major element and HREE compositions are most severely affected by the metasomatic event that led to the crystallization of opx. This process probably involved complex melt– or fluid–rock interaction, but we do not have enough constraints to adequately model this event. We therefore use a simplified approach of bulk addition of opx. Because of the low abundances of HREE in opx, opx addition does not significantly affect the whole-rock HREE budget. Trace element modelling was performed to evaluate the depth and extent of melting experienced by the Kaapvaal Type I samples. We used perfect fractional polybaric non-modal melting of a pyrolitic source adapted after Johnson *et al.* (1990) and Hellebrand *et al.* (2002). As all the peridotites studied here are variably enriched in strongly incompatible elements by metasomatic processes, we model the HREE of the least metasomatized Type I samples. To do so, we assume that the positive slope in the HREE and the low HREE concentrations in these samples are relicts from the original melting event (e.g. Kelemen *et al.*, 1998). The results from the modelling are shown together with the reconstructed REE patterns of garnet-facies Type I samples and the measured REE pattern of K6 (spinel-facies Type I) in Fig. 16. The extremely low HREE

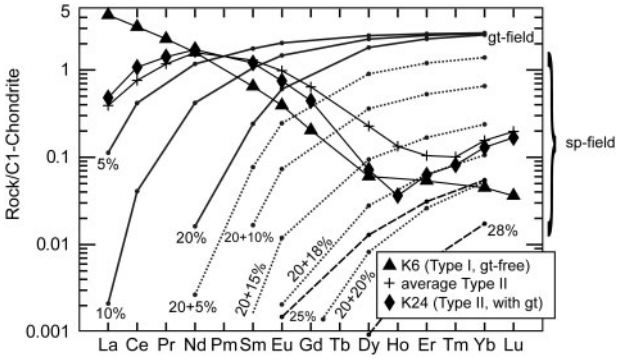

Fig. 16. C1 chondrite-normalized (McDonough & Sun, 1995) REE diagram showing the results of trace element modelling. Continuous lines indicate melting in the garnet stability field only; dotted lines show melting in the garnet field followed by melting in the spinel stability field; dashed lines indicate melting in the spinel stability field only. Source composition for pyrolite from McDonough & Sun (1995). Source modes, melting modes, K_d values and results of the calculations are given in Electronic Appendix Table B3. [See Hellebrand *et al.* (2002) for the conversion of residua from the garnet to the spinel stability field.]

contents of Type I samples require a significant proportion of melting to take place in the absence of garnet. The model shows that the HREE concentrations of K24, or an average Type I sample, can be reproduced by >25% melting in the spinel stability field. However, we cannot exclude the possibility that some melting took place in the garnet field, followed by 15–20% (or more) melting in the spinel stability field. Garnet-free Type I samples (e.g. K6) have even lower HREE contents than garnet-bearing Type I. The very low Yb_N (0·035) of this sample requires even more extensive melting in the absence of garnet. Together with the depleted major element characteristics of K6 (<0·3 wt% CaO and <0·85 wt% Al_2O_3), this points to an origin of this (and other spinel peridotites) as a residue of >30% partial melt extraction at relatively shallow levels. After melting, the residue would have been a spinel- and cpx-free harzburgite with approximately >75% modal olivine and <25% modal opx [model residue after 28% melt extraction in spinel stability field only, applying the melting modes of Johnson *et al.* (1990)]. In contrast, K6 contains 65% olivine and 34% opx (plus <1% exsolved spinel and cpx), indicating opx addition some time after melt extraction.

The above conclusions are supported by Yb–Ca and moderately incompatible element systematics (Kelemen *et al.*, 1998; Canil, 2004). Samples LET2, K18 and GP402 have higher whole-rock Yb than the main Type I cluster. This might indicate that they melted at higher average pressures or experienced later Yb (HREE) addition.

In Fig. 17, bulk-rock major element compositions of the Kimberley and Lesotho samples are plotted together with experimental melting trends at 1, 3 and 7 GPa (Jaques & Green, 1980; Walter, 2003) and trajectories

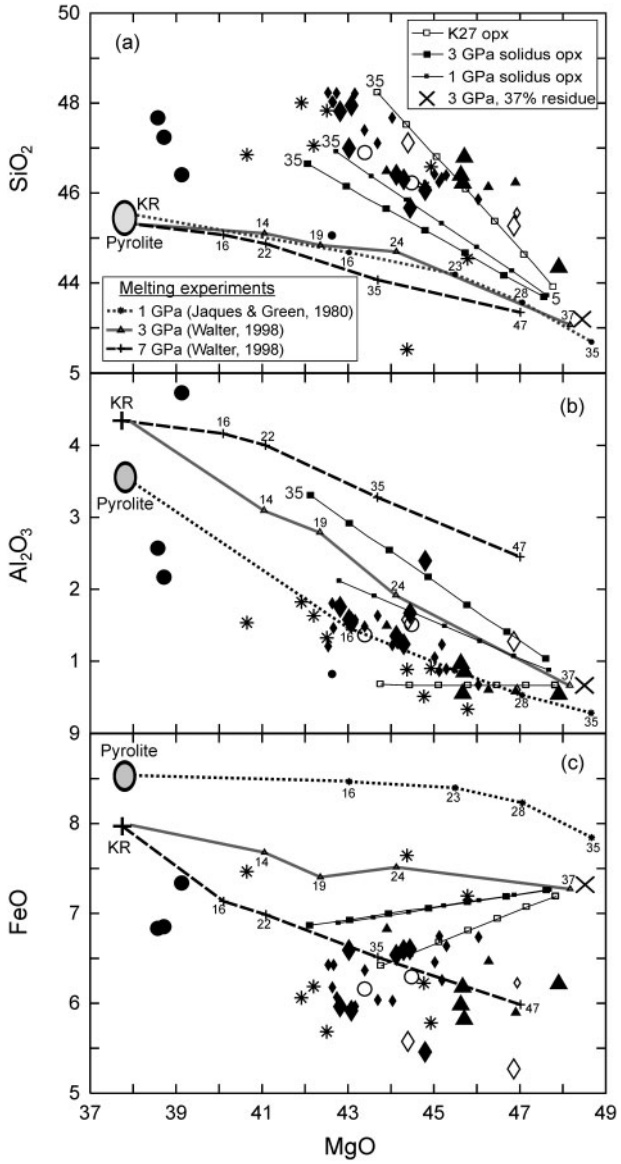

Fig. 17. Comparison of Kimberley and Lesotho major element whole-rock compositions (Table 2 and Simon *et al.*, 2003) with experimental melting trends of pyrolite at 1 GPa (Jaques & Green, 1980) and West Kettle River lherzolite KR4003 (KR) at 3 and 5 GPa (Walter, 1998). Small numbers indicate percentage of melting. Also shown are three trajectories for bulk addition of 5–35% K27opx, an opx from experiment 30.05 of Walter (Walter, 1998) at 3 GPa, 1500°C and an opx from experiment 36 of Wasylenki *et al.* (2003) at 1 GPa, 1250°C to a 37% melting residue of KR at 3 GPa. The opx (K27, 3 GPa, 1 GPa) have wt% MgO: 34·9, 30·2, 32·2; SiO_2: 57·8, 53·3, 54·0; Al_2O_3: 0·7, 8·2, 4·8; FeO: 4·7, 6·0, 6·1. (a) MgO vs SiO_2; (b) MgO vs Al_2O_3; (c) MgO vs FeO. Symbols are as in Fig. 15.

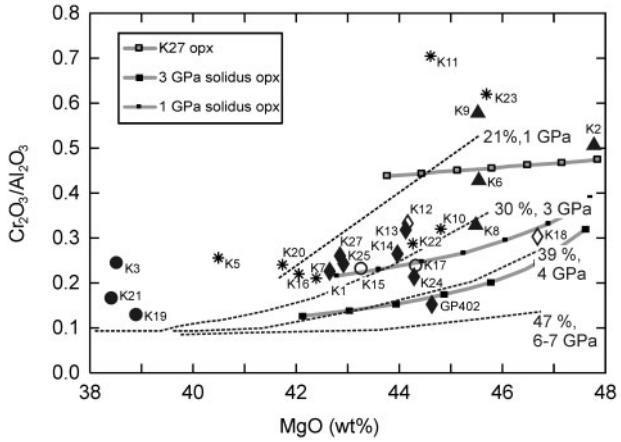

Fig. 18. Cr_2O_3/Al_2O_3 ratio vs MgO wt% in the whole-rocks. The dashed lines indicate experimental residue compositions for increasing degrees of melting at 1 (Wasylenki *et al.*, 2003), 3, 4 and 6–7 GPa (Walter, 1998). The end of the lines is marked with the percentage of melt observed in the experiments corresponding to this experimental bulk composition. The grey lines show up to 35% of opx addition (increasing from right to left) to a residue of 37% melting at 3 GPa (Walter, 1998), as in Fig. 17. The MgO content decreases from >48 wt% to 44–42 wt% when opx is added to the hypothetical residue, whereas the decrease in Cr_2O_3/Al_2O_3 strongly depends on the Al_2O_3 content of the added opx.

for 5–35% opx addition to an experimental residue of 37% melt extraction at 3 GPa. In the Kaapvaal xenoliths, SiO_2 is high and FeO is low at a given MgO content relative to non-cratonic peridotites and experimental residua, features that were previously recognized as typical for Kaapvaal (and some Slave and Siberian) low-T peridotites (e.g. Boyd & Mertzman, 1987; Boyd, 1989; Canil, 1991; Herzberg, 1993, 1999; Rudnick *et al.*, 1994; Kelemen *et al.*, 1998; Walter, 1998, 1999; Griffin *et al.*, 1999*a*). The high SiO_2 contents can be explained by 5–35% of opx addition to a residue of 30–40% melting (Fig. 17; Herzberg, 1993, 1999; Walter, 1998). The low FeO and high MgO contents have previously been explained by melting at very high average pressures (30 to >50% melt extraction at 5 to >7 GPa; e.g. Walter, 2003). Al_2O_3–MgO systematics, however, strongly argue against extensive melting at pressures >3 GPa (Fig. 17b) and are consistent with 20–40% melting at average pressures of 1–3 GPa, followed by opx addition. Opx addition also lowers the FeO content in the bulk-rock by up to 1 wt%, but this is not sufficient to explain the extremely low FeO of the samples (Fig. 17c). It is possible that melt– or fluid–rock reaction (instead of just bulk addition of opx) might lead to a stronger reduction in FeO, in particular if this process takes place under more oxidizing conditions, where iron becomes more incompatible in peridotite as a result of a higher proportion of ferric iron (Canil, 2002).

The Cr/Al ratios of the Kimberley xenoliths (Fig. 18) also indicate that the average depth of melting was equivalent to <3 GPa (Bulatov *et al.*, 1991) and that the garnet-free Type I samples probably experienced melting at shallower depths (highest Cr_2O_3/Al_2O_3 ratios) than the garnet-bearing Type I samples.

Kelemen *et al.* (1998) noted the apparent paradox that, despite evidence of extensive low-*P* melting, most of the samples they studied contain abundant garnet. Accepting that the modelling above demonstrates that melt extraction from the now garnet-rich samples ceased in the spinel or even plagioclase stability field, we concur with Kelemen *et al.* (1998) in invoking a second process that (tectonically) re-emplaces them into the garnet stability field. Although some garnet will form during cooling of residual spinel peridotites formed at high temperatures (e.g. Canil, 1991) this process cannot explain the almost ubiquitous presence of garnet in Kaapvaal xenoliths.

We note that the results presented here point to the importance of low-pressure melting in the genesis of the protolith of the cratonic lithosphere. The high-pressure plume melting alternative for the formation of CLM requires very high degrees of melt removal to explain the lack of an aluminous phase on the solidus (Griffin *et al.*, 2003*a*). As shown by Walter (1998), garnet stability on the solidus increases with increasing pressure and garnet would be removed from the residue only at >67% melt extraction at 7 GPa. In contrast, garnet is exhausted by 14% melting at 3 GPa (Walter, 1998). Residua of high-*P* melting are even more deficient in opx than residua of melting at $P < 3$ GPa. Hence any high-*P* model also must rely on a secondary process of opx addition to explain the silica-rich nature of the CLM (Herzberg, 1999). Because the opx involved in the high-pressure models is the crystallization product of high-degree melts, it would have none of the trace element characteristics that we report here for CLM opx. Instead, the observed opx trace element characteristics match those expected for fluids or melts released from subducting slabs into the shallow upper mantle. Such fluids, through melt–rock interaction with previously highly depleted peridotite, would introduce opx in the manner proposed by Kesson & Ringwood (1989), Rudnick *et al.* (1994) and Kelemen *et al.* (1998). Thus, a high-*P* model (e.g. Griffin *et al.*, 2003a) requires extraordinary conditions (mantle potential temperatures >1700°C) for both melting and the process of silica enrichment, yet still fails to explain the trace element characteristics of the Kaapvaal low-*T* peridotites.

MODEL FOR THE FORMATION OF KAAPVAAL CLM

Here we attempt to place the results in a geological context and propose a simplified model that explains the most important of the observed characteristics (Fig. 19). The geochemical evidence is summarized in Table 9.

(1) Melting in an intra-oceanic setting in the Palaeoarchaean results in a residual mantle that is highly depleted in magmaphile major elements and incompatible trace elements. The intra-oceanic setting is suggested by the extensive shallow melting, which implies that melting occurred in an area of very thin lithosphere.

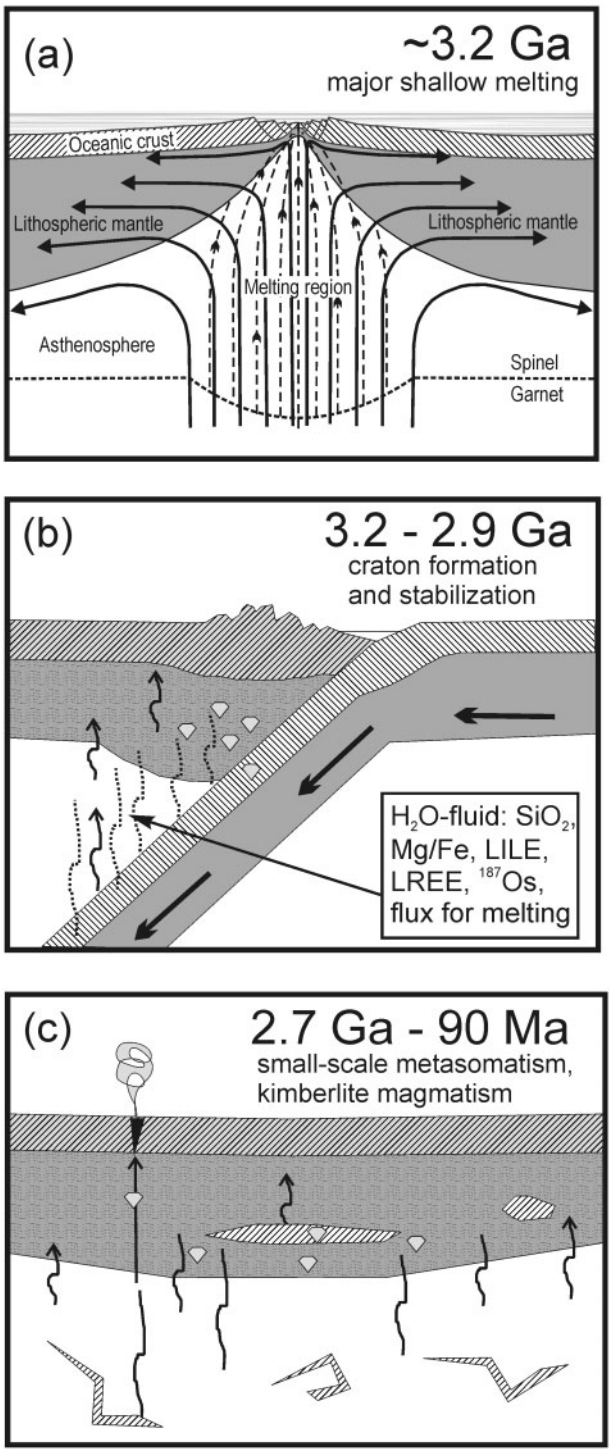

Fig. 19. Schematic geodynamic model for the formation and evolution of the Kaapvaal lithospheric mantle. (See text for explanation and summary in Table 9.)

Table 9: Summary of geochemical characteristics of the Kaapvaal xenoliths and associated geological events

Event	Timing	Evidence/result
(1) Melting at low *P*	~3·5–3·2 Ga	Strong major element and HREE depletion, Cr–Al–V systematics, oldest Archaean Re–Os ages (3·2 Ga)
(2) Hydrous fluid metasomatism +additional melting	~2·9 Ga?	HFSE and HREE depletion, combined with variable enrichment in SiO_2 (opx), LREE and LILE. Archaean Re–Os ages, decoupling of Nd and Hf isotopes leading to negative ε_{Nd} and positive ε_{Hf}
(3) Silicate melt addition	2·9 Ga–120 Ma	High modal garnet and/or cpx contents and enrichment in Fe, Ca, Al, Na, Ti, HREE and HFSE relative to Type I. Younger Re–Os ages, complex Nd–Hf isotope systematics, textural, major and trace element and isotopic disequilibrium between minerals: (a) Ca (cpx) addition: + LREE, Pb, Zr, Hf and Ti, - Zr/Hf. Zr/Hf <PM in Type I samples and K19, >PM in cpx-rich sample K21; (b) Al (garnet) addition: + HREE → high Lu/Hf, more incompatible elements remain low (K19, GP402?)
(4) Kimberlitic metasomatism	120–90 Ma	Introduction of cpx, phl, am, LIMA, Nb, (HREE), Ti, H_2O, carbonate, Hf–Nd isotope variation perpendicular to mantle array

(2) Subduction and collision of small blocks of early crust lead to the formation of a first continental shield (De Wit *et al.*, 1992). This setting provides the opportunity for Si-rich fluids released from the subducted slab to enrich the overlying mantle wedge in Si, LREE and LILE. As a result, the HFSE contents decrease relative to other trace elements, producing the observed high LREE/HFSE ratios. This process can account for the enrichment in Si over Mg and hence the high opx contents in the Kaapvaal upper mantle, and explain the observed correlation between the modal opx content and the Os isotope compositions. The presence of Mesoarchaean eclogitic inclusions in diamonds confirms the presence of subducted material in the Kimberley area at ~2·9 Ga (Richardson *et al.*, 2001; Shirey *et al.*, 2002) as do Archaean ages for Kaapvaal eclogites (Shirey *et al.*, 2001) and for high Re/Os ratio sulphides widely distributed in Kaapvaal peridotites (Griffin *et al.*, 2004; Carlson *et al.*, 2005). Cessation of subduction, attachment of the mantle wedge to the lithosphere and thickening of the whole lithospheric section could have been accomplished by the collision of the western and eastern blocks of the Kaapvaal Craton at ~2·9 Ga (e.g. Jordan, 1988; Schmitz *et al.*, 2004).

(3) Subsequent to the stabilization of the Kaapvaal craton in the late Archaean (~2·8 Ga), the CLM was only locally affected by metasomatic events. With the exception of the Bushveld intrusion (e.g. Carlson *et al.*, 1999), none of these events was sufficient to lead to major modifications of the bulk chemistry of the lithospheric mantle by, for example, the introduction of >10% modal opx, or completely reset the Re–Os system.

Kimberlite magmatism leads to another phase of metasomatism resulting in, amongst other effects, the introduction of cpx. In Lesotho, this event appears to be restricted to Group I kimberlite magmatism in the Cretaceous, whereas multiphase events, including Group II kimberlite volcanism, affect the craton further west in the Kimberley area.

ACKNOWLEDGEMENTS

We thank Gordon Irvine for sharing his Lesotho samples. D. Bell, J. J. Gurney, D. Smith and J. Robey provided invaluable help for successful sampling of the Kimberley dumps. We acknowledge technical help from Wim Lustenhouwer (VU EPMA), Saskia Kars (VU SEM), Bas van der Wagt (VU solution ICP-MS), Paul Mason (Utrecht LA-ICP-MS), Mary Horan (DTM chemistry), Tim Mock (DTM mass spectrometry) and Geoff Nowell (Nd isotopes, Durham). Comments by E.-R. Neumann and the editor M. Wilson on an earlier version of the manuscript helped to improve and shorten it. Thanks also go to J. Davies for redrawing some of the figures. A helpful review by M. Grégoire and two extremely thorough reviews by D. Canil and an anonymous reviewer helped to focus the arguments. The first author was supported by a Ph.D. grant from the Dutch research council (NWO project no. 809-31.001).

SUPPLEMENTARY DATA

Supplementary data for this paper are available at *Journal of Petrology* online.

REFERENCES

Allsopp, H. L. & Barrett, D. R. (1975). Rb–Sr age determinations on South African kimberlite pipes. *Physics and Chemistry of the Earth* **9**, 605–617.

Armstrong, R. A., Compston, W., Retief, E. A., Williams, I. S. & Welke, H. J. (1991). Zircon ion microprobe studies bearing on the age and evolution of the Witwatersrand triad. *Precambrian Research* **53**, 243–266.

Ballhaus, C., Berry, R. F. & Green, D. H. (1991*a*). High-pressure experimental olivine–orthopyroxene–spinel–oxygen geobarometer—implications for the oxidation-state of the upper mantle. *Contributions to Mineralogy and Petrology* **107**, 27–40.

Ballhaus, C., Berry, R. F. & Green, D. H. (1991*b*). Erratum, High-pressure experimental calibration of the olivine–orthopyroxene–spinel–oxygen geobarometer—implications for the oxidation-state of the upper mantle (Vol 107, Pg 27, 1991). *Contributions to Mineralogy and Petrology* **108**, 384.

Becker, H., Carlson, R. W. & Shirey, S. B. (2004). Slab-derived osmium and isotopic disequilibrium in garnet pyroxenites from a Paleozoic convergent plate margin (lower Austria). *Chemical Geology* **208**, 141–156.

Bedini, R.-M., Blichert-Toft, J., Boyet, M. & Albarède, F. (2004). Isotopic constraints on the cooling of the continental lithosphere. *Earth and Planetary Science Letters* **223**, 99–111.

Bell, D. R., Grégoire, M., Grove, T. L., Chatterjee, N., Carlson, R. W. & Buseck, P. R. (2005). Silica and volatile-element metasomatism of Archean mantle: a xenolith-scale example from the Kaapvaal Craton. *Contributions to Mineralogy and Petrology* **150**, 251–267.

Bertrand, P. & Mercier, J.-C. C. (1985). The mutual solubility of coexisting ortho- and clinopyroxene: toward an absolute geothermometer for the natural system. *Earth and Planetary Science Letters* **76**, 109–122.

Bizimis, M., Salters, V. J. M. & Bonatti, E. (2000). Trace and REE content of clinopyroxenes from supra-subduction zone peridotites. Implications for melting and enrichment processes in island arcs. *Chemical Geology* **165**, 67–85.

Boyd, F. R. (1989). Compositional distinction between oceanic and cratonic lithosphere. *Earth and Planetary Science Letters* **96**, 15–26.

Boyd, F. R. & Gurney, J. J. (1986). Diamonds and the African lithosphere. *Science* **232**, 472–477.

Boyd, F. R. & McCallister, R. H. (1976). Densities of fertile and sterile garnet peridotites. *Geophysical Research Letters* **3**, 509–512.

Boyd, F. R. & Mertzman, S. A. (1987). Composition and structure of the Kaapvaal lithosphere, southern Africa. In: Mysen, B. O. (ed.) *Magmatic Processes: Physicochemical Principles. Geochemical Society, Special Publications* **1**, pp. 13–24.

Boyd, F. R. & Nixon, P. H. (1973). Structure of the upper mantle beneath Lesotho. *Carnegie Institution of Washington Yearbook* **72**, 431–445.

Boyd, F. R. & Nixon, P. H. (1975). Origins of the ultramafic nodules from some kimberlites of Northern Lesotho and the Monastery Mine, South Africa. In: Ahrens, L. H., Dawson, J. B., Duncan, A. R. & Erlank, A. J. (eds.) *Proceeding of the First International Conference on Kimberlites, Cape Town, 1973. (Physics and Chemistry of the Earth)*.Oxford: Pergamon Press, pp. 431–454.

Boyd, F. R., Pearson, D. G. & Mertzman, S. A. (1999). Spinel-facies peridotites from the Kaapvaal root. In: Gurney, J. J., Gurney, J. L., Pascoe, M. D. & Richardson, S. H. (eds.) *Proceedings of the 7th International Kimberlite Conference, Cape Town, 1998*. Cape Town: Red Roof Design, pp. 40–48.

Brandon, A. D., Creaser, R. A., Shirey, S. B. & Carlson, R. W. (1996). Osmium recycling in subduction zones. *Science* **272**, 861–863.

Brey, G. P. & Köhler, T. (1990). Geothermobarometry in four-phase lherzolites II. New thermobarometers, and practical assessment of existing thermobarometers. *Journal of Petrology* **31**, 1353–1378.

Bulatov, V., Brey, G. P. & Foley, S. F. (1991). Origin of low-Ca, high-Cr garnets by recrystallization of low-pressure harzburgites. *Fifth International Kimberlite Conference, Extended Abstracts, CPRM Special Publication* **2/91**, 29–31.

Canil, D. (1991). Experimental evidence for the exsolution of cratonic peridotite from high-temperature harzburgite. *Earth and Planetary Science Letters* **106**, 64–72.

Canil, D. (2002). Vanadium in peridotites, mantle redox and tectonic environments: Archean to present. *Earth and Planetary Science Letters* **195**, 75–90.

Canil, D. (2004). Mildly incompatible elements in peridotites and the origins of mantle lithosphere. *Lithos* **77**, 375–393.

Carlson, R. W. & Moore, R. O. (2004). Age of the Eastern Kaapvaal mantle: Re–Os isotope data for peridotite xenoliths from the Monastery kimberlite. *South African Journal of Geology* **107**, 81–90.

Carlson, R. W., Esperanca, S. & Svisero, D. P. (1996). Chemical and Os isotopic study of Cretaceous potassic rocks from southern Brazil. *Contributions to Mineralogy and Petrology* **125**, 393–405.

Carlson, R. W., Pearson, D. G., Boyd, F. R., Shirey, S. B., Irvine, G., Menzies, A. H. & Gurney, J. J. (1999). Re–Os systematics of lithospheric peridotites: implications for lithosphere formation and preservation. In: Gurney, J. J., Gurney, J. L., Pascoe, M. D. & Richardson, S. H. (eds.) *Proceedings of the 7th International Kimberlite Conference, Cape Town, 1998*. Cape Town: Red Roof Design, pp. 99–108.

Carlson, R. W., Irving, A. J., Schulze, D. J., Hearn, J. & Carter, B. (2004). Timing of Precambrian melt depletion and Phanerozoic refertilization events in the lithospheric mantle of the Wyoming Craton and adjacent Central Plains Orogen. *Lithos* **77**, 453–472.

Carlson, R. W., Pearson, D. G. & James, D. E. (2005). Physical, chemical and chronological characteristics of continental mantle. *Reviews of Geophysics* **43**, doi:10.1029/2004RG000156.

Carswell, D. A. (1975). Primary and secondary phlogopites and clinopyroxenes in garnet lherzolite xenoliths. In: Ahrens, L. H., Dawson, J. B., Duncan, A. R. & Erlank, A. J. (eds.) *Proceeding of the First International Conference on Kimberlites, Cape Town, 1973. (Physics and Chemistry of the Earth)*.Oxford: Pergamon Press, pp. 417–429.

Davis, C. L. (1977). The ages and uranium contents of zircons from kimberlites and associated rocks. *Carnegie Institution of Washington Yearbook* **76**, 631–654.

De Wit, M. J., Roering, C., Hart, R. J., Armstrong, R. A., de Ronde, C. E. J., Green, R. W. E., Tredoux, M., Peberdy, E. & Hart, R. A. (1992). Formation of an Archaean continent. *Nature* **357**, 553–562.

Dowall, D. P., Nowell, G. M. & Pearson, D. G. (2003). Chemical pre-concentration procedures for high-precision analysis of Hf–Nd–Sr isotopes in geological materials by plasma ionisation multi-collector mass spectrometry (PIMMS) techniques. In: Holland, J. G. & Tanner, S. D. (eds.) *Plasma Source Mass Spectrometry: Applications and Emerging Technologies*. Cambridge: Royal Society of Chemistry, pp. 321–337.

Drennan, G. R., Robb, L. J., Meyer, F. M., Armstrong, R. A. & de Bruiyn, H. (1990). The nature of the Archaean basement in the hinterland of the Witwatersrand Basin; II, A crustal profile west of the Welkom Goldfield and comparisons with the Vredefort crustal profile. *South African Journal of Geology* **93**, 41–53.

Eggins, S. M., Woodhead, J. D., Kinsley, L. P. J., Mortimer, G. E., Sylvester, P., McCulloch, M. T., Hergt, J. M. & Handler, M. R. (1997). A simple method for the precise determination of ≥40 trace elements in geological samples by ICPMS using enriched isotope internal standardisation. *Chemical Geology* **134**, 311–326.

Eglington, B. M. & Armstrong, R. A. (2004). The Kaapvaal Craton and adjacent orogens, southern Africa: a geochronological database and overview of the geological development of the craton. *South African Journal of Geology* **107**, 13–32.

Ellis, D. J. & Green, D. H. (1979). An experimental study of the effect of Calcium upon garnet–clinopyroxene iron magnesium exchange equilibria. *Contributions to Mineralogy and Petrology* **95**, 499–511.

Erlank, A. J., Waters, F. G., Hawkesworth, C. J., Haggerty, S. E., Allsopp, H. L., Rickard, R. S. & Menzies, M. (1987). Evidence for mantle metasomatism in peridotite nodules from the Kimberley pipes, South Africa. In: Menzies, M. & Hawkesworth, C. J. (eds.) *Mantle Metasomatism*. London: Academic Press, pp. 221–309.

Foley, S. F., Barth, M. G. & Jenner, G. A. (2000). Rutile/melt partition coefficients for trace elements and an assessment of the influence of rutile on the trace element characteristics of subduction zone magmas. *Geochimica et Cosmochimica Acta* **64**, 933–938.

Ganguly, J., Cheng, W. & Chakraborty, S. (1998). Cation diffusion in aluminosilicate garnets: experimental determination in pyrope–almandine diffusion couples. *Contributions to Mineralogy and Petrology* **131**, 171–180.

Godard, M., Bodinier, J.-L. & Vasseur, G. (1995). Effects of mineralogical reactions on trace element redistributions in mantle rocks during percolation processes: a chromatographic approach. *Earth and Planetary Science Letters* **133**, 449–461.

Grégoire, M., Bell, D. R. & Le Roex, A. P. (2002). Trace element geochemistry of phlogopite-rich mafic mantle xenoliths: their classification and their relationship to phlogopite-bearing peridotites and kimberlites revisited. *Contributions to Mineralogy and Petrology* **142**, 603–625.

Grégoire, M., Bell, D. R. & Roex, A. P. L. (2003). Garnet lherzolites from the Kaapvaal Craton (South Africa): trace element evidence for a metasomatic history. *Journal of Petrology* **44**, 629–657.

Griffin, W. L., O'Reilly, S. Y. & Ryan, C. G. (1999*a*). The composition and origin of sub-continental lithospheric mantle. In: Fei, Y., Bertka, C. M. & Mysen, B. O. (eds.) *Mantle Petrology: Field Observations and High Pressure Experimentation: a Tribute to Francis R. (Joe) Boyd. Geochemical Society, Special Publications* **6**, 13–45.

Griffin, W. L., Shee, S. R., Ryan, C. G., Win, T. T. & Wyatt, B. A. (1999*b*). Harzburgite to lherzolite and back again: metasomatic processes in ultramafic xenoliths from the Wesselton kimberlite, Kimberley, South Africa. *Contributions to Mineralogy and Petrology* **134**, 232–250.

Griffin, W. L., O'Reilly, S. Y., Abe, N., Aulbach, S., Davies, R. M., Pearson, N. J., Doyle, B. J. & Kivi, K. (2003*a*). The origin and evolution of Archean lithospheric mantle. *Precambrian Research* **127**, 19–41.

Griffin, W. L., O'Reilly, S. Y., Natapov, L. M. & Ryan, C. G. (2003*b*). The evolution of lithospheric mantle beneath the Kalahari Craton and its margins. *Lithos* **71**, 215–241.

Griffin, W. L., Graham, S., O'Reilly, S. Y. & Pearson, N. J. (2004). Lithosphere evolution beneath the Kaapvaal craton: Re–Os systematics of sulfides in mantle-derived peridotites. *Chemical Geology* **208**, 89–118, doi:10.1016/j.chemgeo.2004.04.002003.

Günther, M. & Jagoutz, E. (1991). Isotopic disequilibria (Sm/Nd, Rb/Sr) between minerals of coarse grained, low temperature peridotites from the Kimberley floors, southern Africa. In: Meyer, H. O. A. & Leonardos, O. H. (eds.) *Proceedings of the 5th International Kimberlite Conference*. Brazilia: Companhia de Pesquisa de Recursos Minerais, pp. 122–124.

Hamilton, M. A., Pearson, D. G., Stern, R. A. & Boyd, F. R. (1998). Constraints on MARID petrogenesis: SHRIMP II U–Pb zircon evidence for pre-eruption metasomatism at Kampfersdam. In: *Extended Abstracts of the 7th International Kimberlite Conference, Cape Town*, pp. 296–298.

Harley, S. L. (1984). An experimental study of the partitioning of iron and magnesium between garnet and orthopyroxene. *Contributions to Mineralogy and Petrology* **86**, 359–373.

Harte, B. (1983). Mantle peridotites and processes – the kimberlite sample. In: Hawkesworth, C. J. & Norry, M. J. (eds.) *Continental basalts and mantle xenoliths*. Nantwich: Shiva Publishing Ltd, pp. 46–91.

Harte, B., Winterburn, P. A. & Gurney, J. J. (1987). Metasomatic and enrichment phenomena in garnet peridotite facies mantle xenoliths from the Matsoku kimberlite pipe, Lesotho. In: Menzies, M. (ed.) *Mantle Metasomatism*. London: Academic Press, pp. 145–220.

Hartnady, C., Joubert, P. & Stowe, C. (1985). Proterozoic crustal evolution in southwestern Africa. *Episodes* **8**, 236–244.

Hawkesworth, C. J., Erlank, A. J., March, J. S., Menzies, M. A. & van Calsteren, P. (1983). Evolution of the continental lithosphere: evidence from volcanics and xenoliths from Southern Africa. In: Hawkesworth, C. J. & Norry, M. J. (eds.) *Continental Basalts and Mantle Xenoliths*. Nantwich: Shiva, pp. 111–138.

Hellebrand, E., Snow, J. E., Hoppe, P. & Hofmann, A. W. (2002). Garnet-field melting and late-stage refertilization in 'residual' abyssal peridotites from the Central Indian Ridge. *Journal of Petrology* **43**, 2305–2338.

Herzberg, C. (1999). Phase equilibrium constraints on the formation of cratonic mantle. In: Fei, Y., Bertka, C. M. & Mysen, B. O. (eds.) *Mantle Petrology: Field Observations and High Pressure Experimentation: a Tribute to Francis R. (Joe) Boyd. Geochemical Society, Special Publications* **6**, 241–257.

Herzberg, C. T. (1993). Lithosphere peridotites of the Kaapvaal Craton. *Earth and Planetary Science Letters* **120**, 13–29.

Hofmann, A. (1988). Chemical differentiation of the Earth: the relationship between mantle, continental crust, and oceanic crust. *Earth and Planetary Science Letters* **90**, 297–314.

Irvine, G. J. (2002). Time constraints on the formation of lithospheric mantle beneath cratons: a Re–Os isotope and platinum group element study of peridotite xenoliths from Northern Canada and Lesotho. Ph.D. thesis, Durham University, Durham.

Irvine, G. J., Pearson, D. G. & Carlson, R. W. (2001). Lithospheric mantle evolution of the Kaapvaal Craton: a Re–Os isotope study of peridotite xenoliths from Lesotho kimberlites. *Geophysical Research Letters* **28**, 2505–2508.

James, D. & Fouch, M. (2002). Formation and evolution of Archaean cratons: insights from southern Africa. In: Fowler, C. M. R., Ebinger, C. J. & Hawkesworth, C. J. (eds.) *The Early Earth: Physical, Chemical and Biological Development. Geological Society, London, Special Publications* **199**, 1–26.

James, D. E., Boyd, F. R., Schutt, D., Bell, D. R. & Carlson, R. W. (2004). Xenolith constraints on seismic velocities in the upper mantle beneath southern Africa. *Geochemistry, Geophysics, Geosystems* **5**, doi:10.1029/2003GC000551.

Jaques, A. L. & Green, D. H. (1980). Anhydrous melting of peridotite at 0–15 kbar pressure and the genesis of tholeiitic basalts. *Contributions to Mineralogy and Petrology* **73**, 287–310.

Johnson, K. T. M., Dick, H. J. B. & Shimizu, N. (1990). Melting in the oceanic upper mantle; an ion microprobe study of diopsides in abyssal peridotites. *Journal of Geophysical Research* **95**, 2661–2678.

Jordan, T. H. (1978). Composition and development of continental tectosphere. *Nature* **257**, 745–750.

Jordan, T. H. (1988). Structure and formation of the continental tectosphere. *Journal of Petrology* **29**, 11–37.

Kelemen, P. B., Hart, S. R. & Bernstein, S. (1998). Silica enrichment in the continental upper mantle via melt/rock reaction. *Earth and Planetary Science Letters* **164**, 387–406.

Kessel, R., Schmidt, M. W., Ulmer, P. & Pettke, T. (2005). Trace element signature of subduction-zone fluids, melts and supercritical liquids at 120–180 km depth. *Nature* **437**, 724–727.

Kesson, S. E. & Ringwood, A. E. (1989). Slab–mantle interactions 2. The formation of diamonds. *Chemical Geology* **78**, 97–118.

Köhler, T. & Brey, G. (1990). Calcium exchange between olivine and clinopyroxene calibrated as geothermobarometer for natural peridotites from 2 to 60 kb with applications. *Geochimica et Cosmochimica Acta* **54**, 2375–2388.

Konzett, J., Armstrong, R. A. & Günther, D. (2000). Modal metasomatism in the Kaapvaal craton lithosphere: constraints on timing and genesis from U–Pb zircon dating of metasomatized peridotites and MARID-type xenoliths. *Contributions to Mineralogy and Petrology* **139**, 704–719.

Krogh, E. J. (1988). The garnet–clinopyroxene iron–magnesium geothermometer—a reinterpretation of existing experimental data. *Contributions to Mineralogy and Petrology* **99**, 44–48.

Lahaye, Y., Arndt, N., Byerly, G., Chauvel, C., Fourcade, S. & Gruau, G. (1995). The influence of alteration on the trace-element and Nd isotopic compositions of komatiites. *Chemical Geology* **126**, 43–64.

Lowry, D., Mattey, D. P. & Harris, J. W. (1999). Oxygen isotope composition of syngenetic inclusions in diamond from the Finsch Mine, RSA. *Geochimica et Cosmochimica Acta* **63**, 1825–1836.

MacGregor, I. (1974). The system MgO–Al_2O_3–SiO_2: solubility of Al_2O_3 in enstatite for spinel and garnet peridotite compositions. *American Mineralogist* **59**, 110–119.

Mattey, D., Lowry, D. & Macpherson, C. (1994). Oxygen-isotope composition of mantle peridotite. *Earth and Planetary Science Letters* **128**, 231–241.

McDonough, W. F. & Sun, S.-S. (1995). The composition of the Earth. *Chemical Geology* **120**, 223–253.

McInnes, B. I. A., McBride, J. S., Evans, N. J., Lambert, D. D. & Andrew, A. S. (1999). Osmium isotope constraints on ore metal recycling in subduction zones. *Science* **286**, 512–516.

Meisel, T., Walker, R. J., Irving, A. J. & Lorand, J.-P. (2001). Osmium isotopic compositions of mantle xenoliths: a global perspective. *Geochimica et Cosmochimica Acta* **65**, 1311–1323.

Menzies, A. H., Carlson, R. W., Shirey, S. B. & Gurney, J. J. (1999). Re–Os systematics of Newlands peridotite xenoliths: implications for diamond and lithosphere formation. In: Gurney, J. J., Gurney, J. L., Pascoe, M. D. & Richardson, S. H. (eds.) *Proceedings of the 7th International Kimberlite Conference*. Cape Town: Red Roof Design, pp. 566–573.

Menzies, M. & Murthy, V. (1980). Enriched mantle: Nd and Sr isotopes in diopsides from kimberlite nodules. *Nature* **283**, 634–636.

Menzies, M. A. & Hawkesworth, C. J. (eds) (1987). *Mantle Metasomatism*. London: Academic Press.

Mibe, K., Fujii, T. & Yasuda, A. (1998). Connectivity of aqueous fluid in the Earth's upper mantle. *Geophysical Research Letters* **25**, 1233–1236.

Mibe, K., Fujii, T. & Yasuda, A. (2002). Composition of aqueous fluid coexisting with mantle minerals at high pressure and its bearing on the differentiation of the Earth's mantle. *Geochimica et Cosmochimica Acta* **66**, 2273–2285.

Morishita, T., Arai, S. & Green, D. H. (2003). Evolution of low-Al orthopyroxene in the Horoman Peridotite, Japan: an unusual indicator of metasomatizing fluids. *Journal of Petrology* **44**, 1237–1246.

Nickel, K. G. & Green, D. H. (1985). Empirical geothermobarometry for garnet peridotites and implications for the nature of the lithosphere, kimberlites and diamonds. *Earth and Planetary Science Letters* **73**, 158–170.

Nowell, G. M., Pearson, D. G., Bell, D. R., Carlson, R. W., Smith, C. B., Kempton, P. D. & Noble, S. R. (2004). Hf isotope systematics of kimberlites and their megacrysts: new constraints on their source regions. *Journal of Petrology* **45**, 1583–1612.

O'Neill, H. S. C. (1980). An experimental study of the iron–magnesium partitioning between garnet and olivine and its calibration as a geothermometer: corrections. *Contributions to Mineralogy and Petrology* **72**, 337.

O'Neill, H. S. C. & Wall, V. J. (1987). The olivine–orthopyroxene–spinel oxygen-geobarometer, the nickel precipitation curve and the oxygen fugacity of the Earth's upper mantle. *Journal of Petrology* **28**, 1169–1191.

O'Neill, H. S. C. & Wood, B. J. (1979). An experimental study of the iron–magnesium partitioning between garnet and olivine and its calibration as a geothermometer. *Contributions to Mineralogy and Petrology* **70**, 59–70.

Pearson, D. G. & Nowell, G. M. (2002). The continental lithospheric mantle: characteristics and significance as a mantle reservoir. *Philosophical Transactions of the Royal Society of London* **360**, 2383–2410.

Pearson, D. G. & Nowell, G. M. (2004). Re–Os and Lu–Hf isotope constraints on the origin and age of pyroxenites from the Beni Bousera peridotite massif: implications for mixed peridotite–pyroxenite mantle sources. *Journal of Petrology* **45**, 439–455.

Pearson, D. G. & Nowell, G. M. (2005). Accuracy and precision in plasma ionisation multi-collector mass spectrometry: Constraints from neodymium and hafnium isotope measurements. In: Holland, J. G. & Bandura, D. R. (eds.) *Plasma Source Mass Spectrometry: Current Trends and Future Developments*. London: Royal Society of Chemistry, pp. 284–314.

Pearson, D. G., Carlson, R. W., Shirey, S. B., Boyd, F. R. & Nixon, P. H. (1995*a*). Stabilization of Archean lithospheric mantle: a Re–Os isotope study of peridotite xenoliths from the Kaapvaal Craton. *Earth and Planetary Science Letters* **134**, 341–357.

Pearson, D. G., Shirey, S. B., Carlson, R. W., Boyd, F. R., Pokhilenko, N. P. & Shimizu, N. (1995*b*). Re–Os, Sm–Nd, and Rb–Sr isotope evidence for thick Archean lithospheric mantle beneath the Siberian Craton modified by multistage metasomatism. *Geochimica et Cosmochimica Acta* **59**, 959–977.

Pearson, D. G., Canil, D. & Shirey, S. B. (2003). Mantle samples included in volcanic rocks: xenoliths and diamonds. In: Carlson, R. W. (ed.) *The Mantle and Core. (Treatise on Geochemistry)*. Amsterdam: Elsevier, pp. 171–275.

Pearson, D. G., Irvine, G. J., Ionov, D. A., Boyd, F. R. & Dreibus, G. E. (2004). Re–Os isotope systematics and Platinum Group Element fractionation during mantle melt extraction: a study of massif and xenolith peridotite suites. *Chemical Geology Special Volume: Highly Siderophile Elements* **208**, 29–59.

Powell, R. (1985). Regression diagnostics and robust regression in geothermometer/geobarometer calibration: the garnet–clinopyroxene geothermometer revisited. *Journal of Metamorphic Geology* **3**, 231–243.

Rapp, R. P., Shimizu, N., Norman, M. D. & Applegate, G. S. (1999). Reaction between slab-derived melts and peridotite in the mantle wedge: experimental constraints at 3·8 GPa. *Chemical Geology* **160**, 335–356.

Richardson, S., Gurney, J., Erlank, A. & Harris, J. (1984). Origin of diamonds in old enriched mantle. *Nature* **310**, 198–202.

Richardson, S., Erlank, A. & Hart, S. (1985). Kimberlite-borne garnet peridotite xenoliths from old enriched subcontinental lithosphere. *Earth and Planetary Science Letters* **75**, 116–128.

Richardson, S. H., Shirey, S. B., Harris, J. W. & Carlson, R. W. (2001). Archean subduction recorded by Re–Os isotopes in eclogitic sulfide inclusions in Kimberley diamonds. *Earth and Planetary Science Letters* **191**, 257–266.

Ringwood, A. (1975). *Composition and Petrology of the Earth's Upper Mantle*. London: McGraw–Hill.

Rudnick, R. L. & Nyblade, A. A. (1999). The thickness and heat production of Archaean lithosphere: constraints from xenolith thermobarometry and surface heat flow. In: Fei, Y., Bertka, C. M. & Mysen, B. O. (eds.) *Mantle Petrology: Field Observations and High Pressure Experimentation: a Tribute to Francis R. (Joe) Boyd. Geochemical Society, Special Publications* **6**, 3–12.

Rudnick, R. L., Donough, W. L. & Orpin, A. (1994). Northern Tanzanian peridotite xenoliths: a comparison with Kaapvaal peridotites and inferences on metasomatic interactions. In: Meyer, H. O. A. & Leonardos, O. H. (eds.) *Kimberlites, Related Rocks and Mantle Xenoliths. Companhia de Pesquisas de Recursos Minerais Special Publication* **Jan/94**, 336–353.

Rudnick, R. L., McDonough, W. F. & O'Connell, R. J. (1998). Thermal structure, thickness and composition of continental lithosphere. *Chemical Geology* **145**, 395–411.

Schmidberger, S. S. & Francis, D. (2001). Constraints on the trace element composition of the Archaean mantle root beneath Somerset Island, Arctic Canada. *Journal of Petrology* **42**, 1095–1117.

Schmidberger, S. S., Simonetti, A., Francis, D. & Gariépy, C. (2002). Probing Archean lithosphere using the Lu–Hf isotope systematics of peridotite xenoliths from Somerset Island kimberlites, Canada. *Earth and Planetary Science Letters* **197**, 245–259.

Schmitz, M. D. (2002). Geological and thermochronological evolution of the lower crust of southern Africa. Ph.D. thesis, Massachusetts Institute of Technology, Cambridge, MA, 269 pp.

Schmitz, M. D., Bowring, S. A., de Wit, M. J. & Gartz, V. (2004). Subduction and terrane collision stabilize the western Kaapvaal craton tectosphere 2·9 billion years ago. *Earth and Planetary Science Letters* **222**, 363–376.

Shimizu, N. (1999). Young geochemical features in cratonic peridotites from Southern Africa and Siberia. In: Fei, Y., Bertka, C. M. & Mysen, B. O. (eds.) *Mantle Petrology: Field Observations and High-pressure Experimentation: a Tribute to Francis R. (Joe) Boyd. Geochemical Society, Special Publications* **6**, 47–55.

Shimizu, N., Pokhilenko, N. P., Boyd, F. R. & Pearson, D. G. (1999). Trace element characteristics of garnet dunites/harzburgites, host rocks for Siberian peridotitic diamonds. In: Gurney, J. J., Gurney, J. L., Pascoe, M. D. & Richardson, S. H. (eds.) *Proceedings of the 7th International Kimberlite Conference, Cape Town, 1998*. Cape Town: Red Roof Design, pp. 773–782.

Shirey, S., Harris, J., Richardson, S., Fouch, M., James, D., Cartigny, P., Deines, P. & Viljoen, F. (2002). Seismic structure, diamond geology and evolution of the Kaapvaal–Zimbabwe craton. *Science* **297**, 1683–1686.

Shirey, S. B., Carlson, R. W., Richardson, S. H., Menzies, A., Gurney, J. J., Pearson, D. G., Harris, J. W. & Wiechert, U. (2001). Archean emplacement of eclogitic components into the lithospheric mantle during formation of the Kaapvaal Craton. *Geophysical Research Letters* **28**, 2509–2512.

Simon, N. S. C. (2004). The formation and modification of cratonic lithospheric roots—a petrological and geochemical study of xenoliths from the Kaapvaal craton. Ph.D. thesis, Vrije Universiteit Amsterdam, 251 pp.

Simon, N. S. C., Irvine, G. J., Davies, G. R., Pearson, D. G. & Carlson, R. W. (2003). The origin of garnet and clinopyroxene in 'depleted' Kaapvaal peridotites. *Lithos* **71**, 289–322.

Smith, C. B. (1983). Pb, Sr and Nd isotopic evidence for sources of southern African Cretaceous kimberlites. *Nature* **304**, 51–54.

Smith, D. (1999). Temperatures and pressures of mineral equilibration in peridotite xenoliths: review, discussion, and implications. In: Fei, Y., Bertka, C. M. & Mysen, B. O. (eds.) *Mantle Petrology: Field Observations and High-pressure Experimentation: a Tribute to Francis R. (Joe) Boyd. Geochemical Society, Special Publications* **6**, 171–188.

Smith, D., Riter, J. C. A. & Mertzman, S. A. (1999). Water–rock interactions, orthopyroxene growth, and Si-enrichment in the mantle: evidence in xenoliths from the Colorado Plateau, southwestern United States. *Earth and Planetary Science Letters* **165**, 45–54.

Sobolev, N. V., Lavrent'ev, Y. U. G., Pokhilenko, N. P. & Usova, L. V. (1973). Chrome-rich garnets from the kimberlites of Yakutia and their paragenesis. *Contributions to Mineralogy and Petrology* **40**, 39–52.

Stachel, T., Aulbach, S., Brey, G. P., Harris, J. W., Leost, I., Tappert, R. & Viljoen, K. S. F. (2004). The trace element composition of silicate inclusions in diamonds: a review. *Lithos* **77**, 1–19.

Stalder, R., Foley, S. F., Brey, G. P. & Horn, I. (1998). Mineral aqueous fluid partitioning of trace elements at 900–1200°C and 3·0–5·7 GPa: new experimental data for garnet, clinopyroxene, and rutile, and implications for mantle metasomatism. *Geochimica et Cosmochimica Acta* **62**, 1781–1801.

Stalder, R., Ulmer, P., Thompson, A. & Günther, D. (2001). High pressure fluids in the system $MgO–SiO_2–H_2O$ under upper mantle conditions. *Contributions to Mineralogy and Petrology* **140**, 607–618.

Van Achterbergh, E., Griffin, W. L. & Stiefenhofer, J. (2001). Metasomatism in mantle xenoliths from the Letlhakane kimberlites: estimation of element fluxes. *Contributions to Mineralogy and Petrology* **141**, 397–414.

Van Orman, J. A., Grove, T. L. & Shimizu, N. (2001). Rare earth element diffusion in diopside: influence of temperature, pressure, and ionic radius, and an elastic model for diffusion in silicates. *Contributions to Mineralogy and Petrology* **141**, 687–703.

Van Orman, J. A., Grove, T. L., Shimizu, N. & Layne, G. D. (2002). Rare earth element diffusion in a natural pyrope single crystal at 2·8 GPa. *Contributions to Mineralogy and Petrology* **142**, 416–424.

Vervoort, J. D. & Blichert-Toft, J. (1999). Evolution of the depleted mantle: Hf isotope evidence from juvenile rocks through time. *Geochimica et Cosmochimica Acta* **63**, 533–556.

Walker, R. J., Carlson, R. W., Shirey, S. B. & Boyd, F. R. (1989). Os, Sr, Nd, and Pb isotope systematics of southern African peridotite xenoliths: implications for the chemical evolution of subcontinental mantle. *Geochimica et Cosmochimica Acta* **53**, 1583–1595.

Walter, M. J. (1998). Melting of garnet peridotite and the origin of komatiite and depleted lithosphere. *Journal of Petrology* **39**, 29–60.

Walter, M. J. (1999). Melting residues of fertile peridotite and the origin of cratonic lithosphere. In: Fei, Y., Bertka, C. M. & Mysen, B. O. (eds.) *Mantle Petrology: Field Observations and High-pressure Experimentation: a Tribute to Francis R. (Joe) Boyd. Geochemical Society, Special Publications* **6**, 225–239.

Walter, M. J. (2003). Partial melting. In: Carlson, R. W. (ed.) *Treatise on Geochemistry*. Amsterdam: Elsevier, pp. 1–33.

Wasylenki, L. E., Baker, M. B., Kent, A. J. R. & Stolper, E. M. (2003). Near-solidus melting of the shallow upper mantle: partial melting experiments on depleted peridotite. *Journal of Petrology* **44**, 1163–1191.

Wells, P. R. A. (1977). Pyroxene thermometry in simple and complex systems. *Contributions to Mineralogy and Petrology* **62**, 129–139.

Widom, E., Kepezhinskas, P. & Defant, M. (2003). The nature of metasomatism in the sub-arc mantle wedge: evidence from Re–Os isotopes in Kamchatka peridotite xenoliths. *Chemical Geology* **196**, 283–306.

Witt-Eickschen, G. & Seck, H. A. (1991). Solubility of Ca and Al in orthopyroxene from spinel peridotite: an improved version of an empirical geothermometer. *Contributions to Mineralogy and Petrology* **106**, 431–439.

Yaxley, G. M. & Green, D. H. (1998). Reactions between eclogite and peridotite: mantle refertilization by subduction of oceanic crust. *Schweizerische Mineralogische und Petrographische Mitteilungen* **78**, 243–255.

Zack, T., Foley, S. F. & Jenner, G. A. (1997). A consistent partition coefficient set for clinopyroxene, amphibole and garnet from laser ablation microprobe analysis of garnet pyroxenites from Kakanui, New Zealand. *Neues Jahrbuch für Mineralogie, Abhandlungen* **172**, 23–41.

Zhang, H.-F., Menzies, M. A. & Mattey, D. (2003). Mixed mantle provenance: diverse garnet compositions in polymict peridotites, Kaapvaal craton, South Africa. *Earth and Planetary Science Letters* **216**, 329–346.